Non-Intrusive Engine Piston Temperature Measurement Using a Fiber Bragg Grating

by

Timothy Ross Pfeifer

A thesis submitted in partial fulfillment

of the requirements for the degree of

Master of Science

(Mechanical Engineering)

at the

University of Wisconsin – Madison

2006

Approved: _____

Jaal B. Ghandhi
Principal Advisor
Associate Professor, Mechanical Engineering
University of Wisconsin – Madison

Date: _____

Abstract

An embedded fiber Bragg grating was used to examine the operating temperature of a small gasoline engine piston. Optical system analyses were conducted to enhance the accuracy and consistency of the measured piston temperature. The goal of the work was to experimentally characterize light transmission through embedded fibers, with the aim of improving the entire measurement system to acquire data as the engine was running.

An aspheric collimating lens and a polyimide-buffered fiber Bragg grating were found to create a transmission profile with a much more noticeable Bragg dip, and the optical system was more tolerant to misalignment while maintaining measurement accuracy. A wavelength-agile VCSEL diode laser provided a low-cost means to interrogate the embedded fiber Bragg grating at speeds up to 100 kHz, albeit for a small wavelength domain.

Stationary engine measurements successfully determined the piston temperature to be 31.5 °C. However, irreparable damage was caused to the engine when a small piece of electroplated nickel became loose and wedged between the piston and cylinder wall shortly after initiating motored tests. After verifying the integrity of the embedded FBG, the cylinder was rebored and the piston reinstalled. A modified motoring experiment proved that light coupling was occurring for each engine rotation, and analysis determined the piston temperature to be approximately 56 °C. Due to substantial noise in the photodetector data, it was difficult to qualitatively identify the Bragg wavelength without making assumptions about the expected Bragg dip location.

Acknowledgements

This grand undertaking has only been possible by support and encouragement from a number of great people. There are too few words to express my thanks for all you have done. I am sure that without the constant love from my family, I would surely have abandoned this project many times. Mom, Dad, Joe and Carolyn: Thank you for always believing in me and showing me more about who I really am.

My advisor, Dr. Jaal Ghandhi, provided his knowledge and insight at the many difficult points in this project, and all the points in between. I have been challenged to think critically at each step, and while I didn't always agree, I have seen the benefits of the perseverance he has encouraged in me. Thank you also to Professors Scott Sanders and Xiaochun Li for assisting me along the way and serving on my thesis committee.

The Wisconsin Small Engine Consortium (WSEC) sponsored my project and provided funding for the various equipment required. The member companies of Briggs & Stratton, Harley-Davidson, Kohler, Mercury Marine, MotoTron, Fleetguard and the Wisconsin Department of Commerce continue to assist research at the Engine Research Center.

The large part of my lab experience was taught to me by Dennis Ward and Nate Haugle. I learned all the intricacies of engine assembly and laboratory setup from them and now feel comfortable attempting to crack open an engine and get my hands dirty. In addition, the students in Scott's optics group answered all of my seemingly simple optics questions and guided me to the parts I needed. Thanks Chris, Laura, Drew, Renata, and Karissa.

Thank you to Susie Strzelec and Deanna Duerst for handling administrative tasks efficiently. Similar thanks to Ralph Braun and Will Lokke for helping me find the tools and equipment I needed to get my lab in order.

Finally, I thank God for guiding me to the University of Wisconsin and providing me with the strength and encouragement to survive and succeed here. The blessings of friends, family, health and abundance are all His doing and I am exceedingly grateful.

Table of Contents

List of Figures

List of Tables

1 Introduction

1.1 Motivation

The internal combustion (IC) engine represents one of the most important and critical technologies in society today. These engines provide the locomotive forces responsible for powering the approximately 600 million automobiles in the United States alone. However, the requirements of the Clean Air Acts of 1970 and 1990, and subsequent standards since then have placed tighter demands on vehicle emissions, while consumers continue to demand comparable, if not increased, performance. This combination has led manufacturers to explore engine systems for every area of improvement and has pushed these systems to their mechanical and material limits.

Of these engine systems, the two-stroke and air-cooled designs experience the most stressful thermal loading. As new engines are designed, it has become increasingly necessary to ensure optimal heat fluxes through the combustion chamber surfaces, most notably the head, cylinder liner and piston. A number of different measurement systems have been developed to determine the operating temperature of the piston. However, these systems are noticeably intrusive, and many add a significant amount of mass to the piston. It is therefore of interest to design and develop a non-intrusive measurement device capable of withstanding the harsh environment in the engine while providing accurate and reliable temperature data.

1.2 Research Objectives

The purpose of the research experiments here are to investigate piston temperature using a newly developed sensor: an embedded fiber Bragg grating (FBG). Fiber Bragg gratings are sensitive to temperature and strain, with the added benefit of immunity to electric and magnetic interference. In addition, the measured quantity of a fiber Bragg grating is the Bragg, or center, wavelength and not a type of power measurement. This eliminates many of the tedious alignment and error analyses common in power measurements, and provides a more absolute means of measuring specific information, in this case engine piston temperature.

With the development of new sensors such as the fiber Bragg grating, measurements once unobtainable are now becoming possible. By embedding these sensors at the precise location in a material or structure where measurements are needed, reliable and accurate data is able to be collected in real-time.

The primary thrust of this research is directed towards improving the system developed by Ward [24]. Ward was able to use this method to successfully measure engine piston temperature. However, there were a number of difficulties experienced in the experiments performed. It is desired that this system be able to provide accurate and reliable temperature data while the engine is running. Thus, concern is given in this research to improving the accuracy of the temperature measurements, as well as improving the entire measurement system to acquire data as the engine is running.

2 Background

2.1 Piston Heat Transfer and Thermal Theory

While all of the components in an internal combustion engine experience significant thermal and mechanical stresses, the piston represents one of the components operating under the most unfavorable conditions [1]. An increase in piston temperature may lead to a reduction in engine durability. Increased piston temperatures lead to increased in-cylinder temperatures, which affect the performance of the lubricating oil, as well as wear and thermal loading of engine components, which are already pushed to the material property limits [32]. During operation, the piston is exposed to peak burned gas temperatures of ~2500 K and heat fluxes as high as 10 MW / m^2 [2], as well as dynamic forces as great as 2000 g's. At these high burned gas temperatures, very few materials would be able to survive or maintain their material properties. In order to prevent piston failure, piston temperatures must be kept near or below ~300 ºC for aluminum alloys. This requirement places limitations on engine design and configuration, and limits engine performance characteristics, such as power, torque, and fuel consumption.

The magnitude of engine heat transfer is affected by many engine variables, including engine speed, load, equivalence ratio, compression ratio, spark timing, swirl or squish motion, mixture inlet temperature, coolant temperature and composition, wall material and wall deposits. Of these variables, speed and load have the greatest effect on heat flux in the engine. High surface temperatures, especially piston temperatures, can contribute to knock,

which causes severe vibrations and forces in the engine, leading to increased material stresses and premature material failure.

2.2 Experimental Piston Temperature Measurements

To examine the heat transfer effects in an internal combustion engine and to determine piston material fatigue, a number of different measurement techniques have been employed to obtain the operating temperature of the engine piston. The measurement of piston temperature in a reciprocating engine has historically been a very time-consuming and expensive process [3]. The measurement system must be able to withstand large inertial forces, high temperatures, and exposure to a gas and oil environment [4]. In addition, a system is sought that is easy to install, self- or non-powered, continuously reading, fast responding, and durable [5]. The techniques and systems developed and implemented thus far can be categorized as either contact or non-contact methods.

2.2.1 Contact Methods

One of the first piston temperature measurement methods employed used embedded thermocouples in the piston [6, 7]. The lead wires from the thermocouples were routed below the piston to the crankcase. Here the wires were passed out of the engine and connected to the compensating cold junction and voltmeter. In the case of Furuhama *et. al.* [6], a mechanical linkage was initially installed, which resulted in snapping of the thermocouple wires. To overcome this problem, a large radius spring to which the thermocouples wires were attached was installed. Practically, this method was useful for engine speeds up to 4000 RPM. In order to achieve higher speeds, a method was employed

that routed the thermocouple wires up through a conduit in the combustion chamber and out of the engine through the head [6]. Using this method, measurements were taken on a 2-cycle engine without breakage and snapping of the wire for engine speeds up to 8000 RPM.

While routing the thermocouple wires through the combustion chamber makes the method more durable, it affects the very nature of combustion and heat transfer in the engine cylinder. In an effort to avoid these effects, the wired thermocouple method has been modified. The first modification was to terminate the thermocouple wires as contacts on the piston and install similar contacts in the engine crankcase [8, 9, 10, 11]. With these contacts, the electrical circuit closes once per revolution, permitting a measurement. Successful measurements were taken for engine speeds up to 2600 RPM [10]. At this point, the circuit contacts begin to bounce, causing an erratic measurement. By changing the contacts in the crankcase to sliding contacts, a more reliable circuit was established because sliding contacts provide a longer time for the circuit to be closed. Using this method, temperatures were successfully measured for engine speeds of 3000 RPM.

Another useful and simple measurement device is the Templug. A Templug is a temperature sensitive steel set screw that changes hardness when exposed to a high temperature environment [14]. There is no other instrumentation necessary for this measurement. However, this method is only able to determine the maximum temperature of a component and is incapable of detecting time-dependent and unsteady temperatures. The accuracy of this temperature measurement is dependent on the amount of time spent at the maximum temperature. It is recommended that at least 25% of the operating time be spent at the maximum temperature. Once tempered, the Templugs are returned to the manufacturer,

where the hardness change of the alloy and the exposure time determine the maximum temperature.

2.2.2 Non-Contact Methods

While the aforementioned methods have worked in engine environments, most required careful rigging and difficult experimental adjustment [5]. As a result, measurement techniques were developed that avoided any type of contacts or continuously wired circuits.

One of the first wireless methods developed relied on radio frequency (RF) telemetry [3, 5]. A self-powered circuit, called a single transistor blocking oscillator, transmits a frequency defined by

$$f(C) = \frac{1}{2\pi\sqrt{LC}} \qquad (2.1)$$

where L is the inductance of the transmitter antenna coil and C is the capacitance value of the sensing capacitor (shown as L1 and C1, respectively, in Figure 2.1).

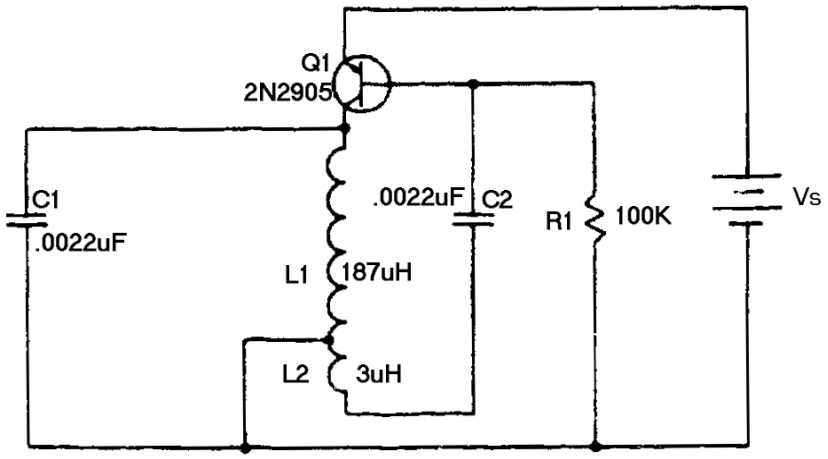

Figure 2.1. Basic transmitter circuit for radio frequency telemetry system. Reprinted from [3].

The sensing capacitor is temperature sensitive and is the sensing element for the temperature measurement in this system. As the capacitance of the sensor changes with temperature, the transmitted frequency also changes. The shift in frequency is linearly proportional to the temperature change:

$$f(T) = \frac{T}{2\pi\sqrt{LK}}, \qquad 2\pi\sqrt{LK} = \text{constant}, \; K = \text{dielectric constant of capacitor} \qquad (2.2)$$

To power this system, a novel power generator was designed. Utilizing electromagnetic induction, a magnet is allowed to slide in a coil of wire, shown below in Figure 2.2.

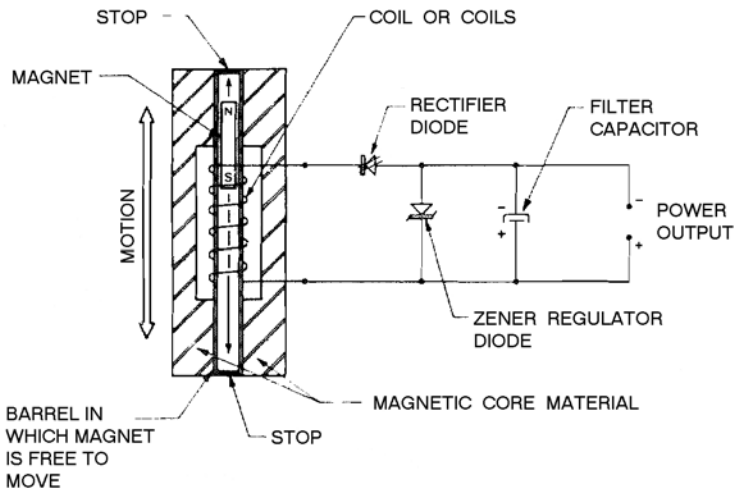

Figure 2.2. Electromagnetic power generator for RF transmitter circuit. Reprinted from [5].

With the transmitter circuit providing a radio frequency, a receiver antenna is placed in or near the engine. The receiver antenna is simply a loop of wire connected to a measurement system. Given a calibration curve for frequency versus temperature, the piston temperature can be determined. This technique was successfully operated at engine speeds up to 5000 RPM and temperatures up to 120 ºC. However, the transmitter circuit was subject to failure at operating temperatures above 150 ºC.

Another telemetric technique for piston temperature measurement incorporated the use of an infrared light transmitter. Infrared light pulses are transmitted through the mist of oil, air and exhaust in the crankcase of a two-stroke engine to a photodetector [4]. These pulses are able to penetrate the mist and are immune to electrical and magnetic interference. These pulses are continuously transmitted, resulting in a real time measurement system. The temperature sensing circuit converts the voltage signal from the embedded thermocouples to a modulated voltage pulse train, which drives an infrared LED. The infrared pulses are then

detected by a phototransistor mounted in the crankcase and are converted back to voltage signals, which can be read on an oscilloscope, voltmeter, or stored by a data acquisition system. The transmitting circuit was powered by two 3.6 volt lithium-thionyl batteries attached to the engine piston. These cells were chosen for their stability in a temperature environment of 150 ºC. An illustration of this infrared system is shown in Figure 2.3.

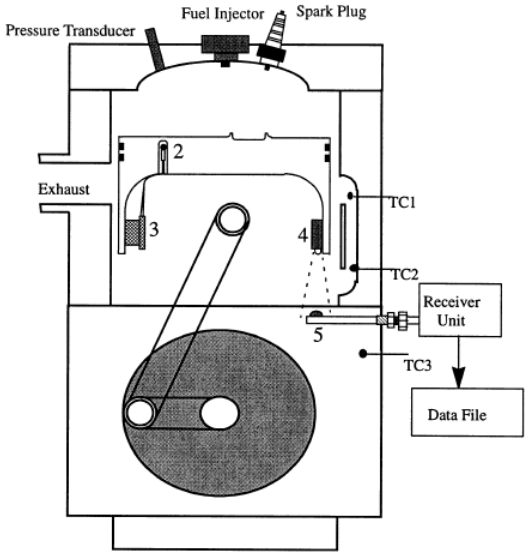

Figure 2.3. Infrared telemetry system mounted in two-stroke engine. Reprinted from [12].

Experiments conducted with this measurement system were successful for engine speeds up to 5000 RPM. Measured temperature data had an accuracy of ±2.8 ºC for operating temperatures between 90 and 150 ºC. The tests demonstrate the system is capable of withstanding operating temperatures of 150 ºC.

These telemetry methods, both the radio frequency and the infrared light, have significant advantages over the previous thermocouple methods. However, these systems add a significant amount of mass to the piston assembly, affecting the piston dynamics and thermal loading under consideration.

Another novel non-contact measurement concept involved an electromagnetic (EM) induction method. The induction section involves a pair of transmitter and receiver coils installed beneath the piston in the cylinder, and a resonator coil installed on the piston, shown in Figure 2.4 [13]. The resonator coil is wired to the embedded Thermistor in the engine piston.

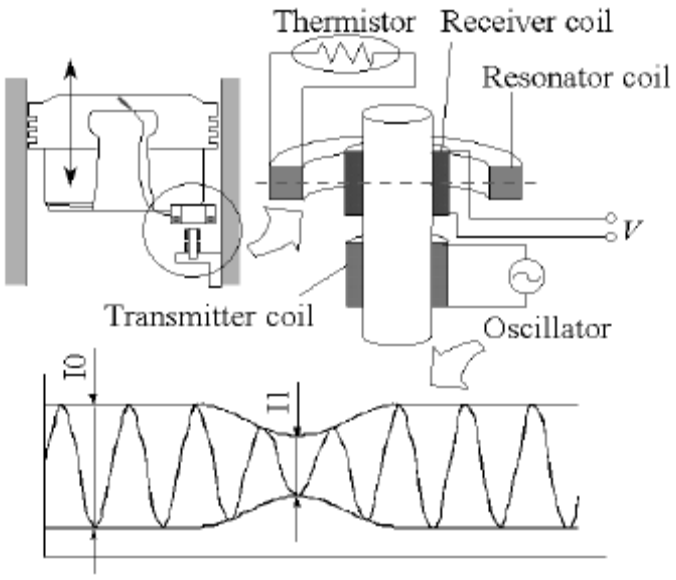

Figure 2.4. EM induction system. Reprinted from [13].

An applied current in the transmitter coil will generate a magnetic field and a current (I_0 in Figure 2.4), which will be the same as in the receiver coil. When the resonator coil reaches bottom dead center (BDC), it concentrically crosses the receiver coil and has a current electromagnetically induced in it by the receiver coil. Due to the nature of the Thermistor, its resistance will drop as its temperature rises, causing a lower electric current (I_1 in Figure 2.4) in the receiver coil. As a result, the temperature of the Thermistor can be

determined by comparing the actual current ratio $\frac{I_1}{I_0}$ with pre-developed temperature curves, or to other current ratios.

For this system to perform correctly, the resonator and receiver coils are designed so as to avoid any possible contact. In addition, these coils are positioned such that the moving resonator coil will have passed the receiver coil by BDC, insuring a point of maximum EM induction. With these considerations, the EM induction measurement system is capable of measuring temperatures from -40 to 400 °C, with an accuracy of ±2.5 °C and a time resolution of 1.5 sec.

Similar to the telemetry methods, the EM induction system also adds a significant amount of mass to the reciprocating piston, altering the heat transfer and momentum of the piston. To avoid the additional mass of these on-piston non-contact methods, new measurement systems seek to make minor modifications to the devices under consideration, adding minimal mass to the system and remaining minimally intrusive.

2.3 Non-Contact Temperature Measurement Methods

There are a number of novel temperature measurement devices that are beginning to emerge as feasible alternatives to the traditional thermocouple methods mentioned previously. Many of these new techniques rely on optical methods. Of these new techniques, optical fiber Bragg gratings (FBGs) and phosphorescence are further reviewed.

2.3.1 Fiber Bragg Gratings – Theory and Implementation

The discovery of photosensitivity in optical fiber [15] has led to the development of fiber-based sensors. Photosensitivity refers to a permanent change of the index of refraction

of the fiber core when exposed to light with a certain characteristic wavelength and intensity [16]. These new sensors take advantage of the unique features of fiber optic technology including extremely small physical size [17]. One of these new sensors is the fiber Bragg grating.

The fiber Bragg grating (FBG) acts as a wavelength-selective mirror for incoming light. When broadband light is transmitted into the fiber core, the FBG functions like a filter, reflecting light at a single wavelength, called the Bragg wavelength [18]. This filtering yields a single wavelength or narrow wavelength band reflected back through the fiber while the remainder is simply transmitted through the grating. These effects can be seen in the diagrams in Figure 2.5. FBGs are relatively straightforward and inexpensive to produce, and possess highly favorable sensing characteristics, including immunity to optical power fluctuations and electromagnetic interference, low transmission loss, light weight, flexibility, stability, high temperature tolerance, and self-referencing [16, 19, 20]. FBGs are an active research area, owing to a broad range of sensing capabilities, including measurements of stress, strain, displacement, torsion, curvature, angle, pressure, electric current, voltage, and temperature [21].

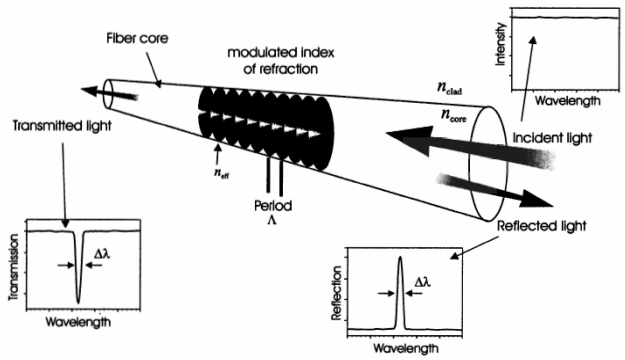

Figure 2.5. Representation of fiber Bragg grating, illustrating the period of the grating, as well as typical profiles for transmitted and reflected light. Reprinted from [16].

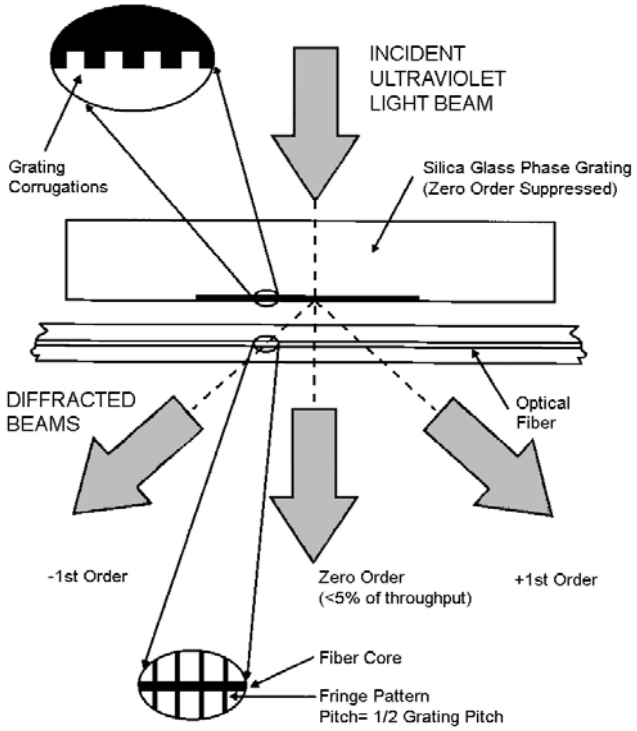

Figure 2.6. Schematic of phase mask technique for imprinting a fiber Bragg grating in a photosensitive optical fiber. Reprinted from [22].

A comparatively simple device, the fiber Bragg grating consists of a periodic modulation of the index of refraction along the fiber core [16]. One of the most effective ways of inscribing a Bragg grating in photosensitive fiber is the phase mask technique. The phase mask is produced as a one dimensional periodic surface-relief pattern with period Λ_{pm} etched into fused silica. The amplitude of the periodic surface-relief pattern approximates a square wave in profile [22]. This profile is chosen such that the zero-order diffracted beam is suppressed to less than 3% of the transmitted power. The $\pm 1^{st}$ order diffracted beams are maximized, each containing ~35% of the transmitted power. Figure 2.6 illustrates the inscription process. The period of the inscribed fringes in the fiber core is half the period of the phase mask fringes:

$\Lambda_{FBG} = ½ \Lambda_{pm}$ (2.3)

As a result of the inscribing process, a fiber Bragg grating is formed in the core of the optical fiber. The first-order Bragg condition is:

$\lambda_B = 2 n_{eff} \Lambda$ (2.4)

where the Bragg wavelength λ_B is the free space center wavelength of the input light back-reflected from the FBG, n_{eff} is the effective refractive index of the fiber core at the free space center wavelength, and Λ is the period of the inscribed fringes. The bandwidth of the reflected signal is typically ~0.05 to 0.3 nm in most sensor applications. It is the structure of a fiber Bragg grating that results in the temperature and strain sensitivity observed through experiments.

The temperature sensitivity of a FBG occurs principally through the effect on the induced refractive index change and, to a lesser extent, on the thermal expansion coefficient of the fiber [20]. An applied strain field directly affects the response of the FBG through the expansion and compression of the grating pitch size and through the strain-optic effect, which is the strain-induced modification of the refractive index. A typical response to applied strain and temperature can be seen in Figure 2.7. Both the strain and temperature response of the FBG are linear and exhibit excellent characteristics for sensing applications.

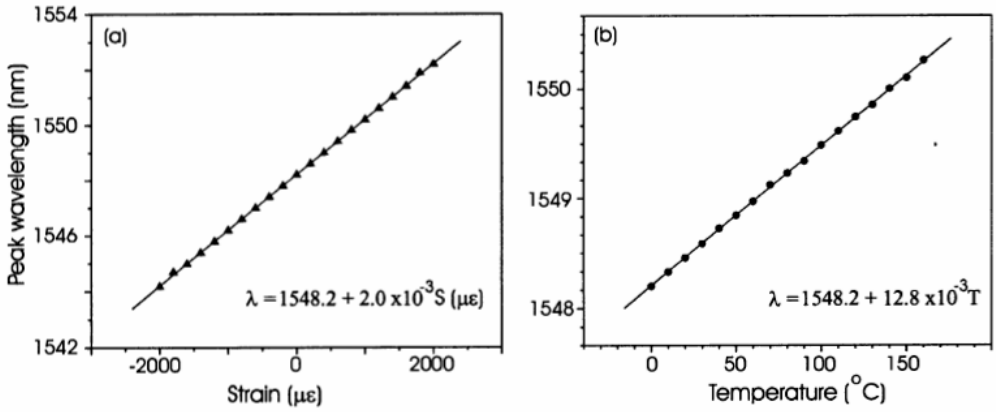

Figure 2.7. Typical strain and temperature affect on wavelength, illustrating the fiber Bragg grating's linear response. Reprinted from [16].

The linear response of a FBG to temperature and strain, coupled with its small physical size, is the motivator to embedding these sensors. These sensors can be used to gain data for validating or improving designs during the prototype stage or to obtain information on the performance and structural integrity of components or structures [18]. Fiber optic sensors embedded within structural materials add intelligence to structures and enable real-time monitoring at some critical locations not accessible to ordinary sensors. The ability to obtain data from materials and structures such as this is important to many industries.

2.3.2 Single Mode and Multimode Comparison

Initially, fiber Bragg gratings were written on single mode fibers, resulting in gratings with high reflectivity and narrow bandwidth [23]. These properties lead to a readily identified Bragg wavelength in a reflection or transmission plot. A single mode FBG has been previously installed in a small engine piston [24], with a certain amount of success. The overall transmission efficiency of the installed system was 83 dB, or 5e-7 %. While a

measurement was still possible with this small amount of light, significant time was spent on system optical alignment. In spite of the characteristically high reflectivity and narrow bandwidth of a single mode FBG, as shown in Figure 2.8, these sensors are not appropriate for use in short distance transmission and measurement systems, due to coupling difficulties arising from a small core diameter. To increase the overall light transmission through the system, a multimode (MM) FBG could be considered.

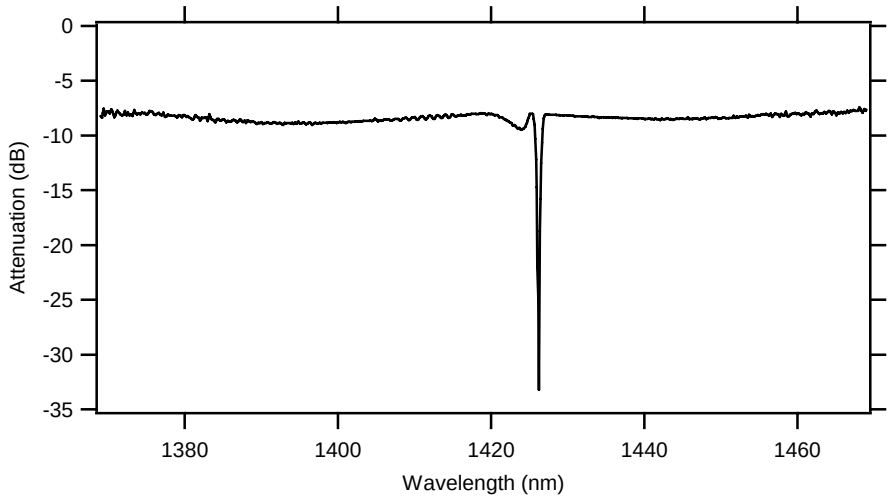

Figure 2.8. Light transmission through single mode FBG.

Multimode FBGs are similar in concept to single mode FBGs, with the difference being the size of the core of the optical fiber. Multimode fiber cores are available in various sizes, from 50 μm up to 1500 μm. A larger fiber core increases the amount of light coupled into the fiber. Multimode FBGs have been investigated as possible temperature sensors, with comparable sensitivity to single mode FBGs. According to Degamber *et. al.* [25], the temperature sensitivity of a multimode FBG was 10.8 pm $°C^{-1}$ with an accuracy of ±0.5 °C, while a single mode FBG had a temperature sensitivity of 5.6 pm $°C^{-1}$ and an accuracy of ±2 °C. While the transmission profiles for MM FBGs is considerably more complicated, the

accuracy remains high. Advanced coupling techniques may make it possible to eliminate some of the Bragg dips in the transmission profile.

2.3.3 Phosphorescence

Fiber Bragg grating technology is an in-fiber technique where relevant data is wavelength encoded. Another optical temperature measurement method relies on the method of phosphorescence. These types of measurement methods may be used in harsh environments, where rigors such as high temperature, EM radiation, or gas and oil mixtures make conventional measurements extremely problematic.

Phosphorescence occurs when a substance is excited by an adequately high intensity light, such as an electron beam or ultraviolet radiation [26, 27]. Electrons in the substance absorb energy from the illuminating light source and reach higher energy states. These electrons can then return to their ground state by emitting excess energy as a photon, either by fluorescence or phosphorescence, which occurs over longer times than fluorescence. In the conventional optical thermometer using fluorescence, temperature is measured based on the temperature dependence of the spectrum. The sensitivity and accuracy of the measurement is influenced greatly by the number of data points acquired and by the curve-fitting procedure [28]. There is another way for the electrons to return to their ground state: by first transitioning to a triplet state before returning to their ground state. The excess energy during the fall from the triplet state is emitted as a photon, known as phosphorescence. Phosphorescence differs from fluorescence in a number of ways, particularly:

1) The elapsed time for the whole process is longer (from 10 s to minutes), making measurement of the emitted light easier.

2) The intensity of the light is lower, requiring a more sensitive light detector.

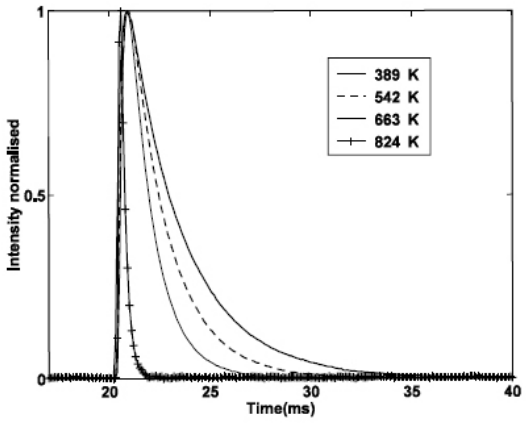

Figure 2.9. Phosphorescence intensity versus time for various temperatures. Reprinted from [27].

In order to develop a highly sensitive and accurate measurement technique, thermographic phosphors must be used, which are phosphors that exhibit temperature dependence in either afterglow intensity or decay lifetime. Afterglow intensity refers to the relative intensity of distinct emission lines of the emitted photons, while decay lifetime refers to the time constant of the exponential decay that occurs after excitation has ceased [28, 29]. Depending on the particular dopant used, each of these thermographic phosphors is very sensitive in a particular narrow temperature region, exhibiting an accuracy of the order 1-5 K. Figure 2.10 below illustrates the temperature sensitive ranges for two different phosphors. Today, a large number of different phosphors are produced, covering a large band of temperatures, from cryogenic temperatures up to 1673 K or higher, making them suitable to many applications [27].

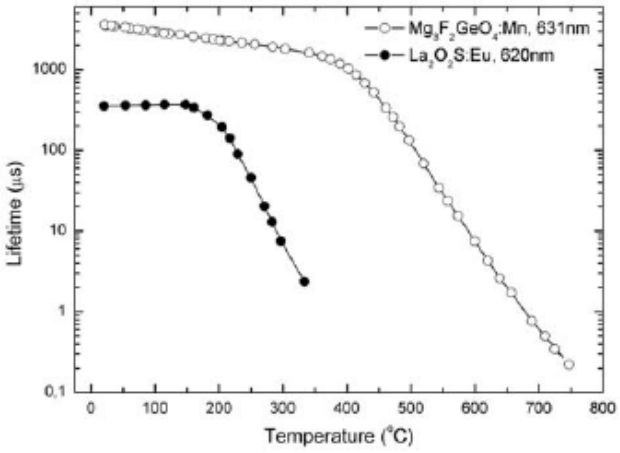

Figure 2.10. Lifetime temperature sensitivity for two different thermographic phosphors. Reprinted from [30].

To infer the temperature from phosphorescence, the time-resolved signal is first fitted to an exponential decay curve, which gives an estimate of the decay lifetime. These curves are then compared to calibration decay curves, yielding the approximate temperature of the phosphor and consequently the temperature of the surface of interest [30]. Since phosphorescent emissions are of low intensity, either a photo-multiplier tube (PMT) or sensitive CCD camera is used to measure the emitted light.

In an experiment conducted by Omrane *et. al* ., laser-induced phosphorescence was used to measure the temperature of the intake and exhaust valves in an internal combustion engine [27]. A simplified schematic of the experiment is shown in Figure 2.11, showing optical access to the valves through a modified engine head. The phosphor was applied to the surfaces of interest using a ceramic binding agent. With these modifications made, laser light was guided onto the coated surfaces and lifetime decay measurements were made. Measured temperatures steadily increased as the valves were heated, until they reached a

steady state temperature of approximately 660 K. A second set of measurements confirmed these results and indicates a certain amount of repeatability.

To adapt this method to measure operating piston temperatures, optical access to the combustion chamber would required either a new hole to be drilled in the head or for one of the valves or 2nd spark plug to be replaced with a window. Using a coating technique similar to that used by Omrane *et. al.*, the phosphor can be applied to the piston surface. Considerations must be given to the accuracy of the measurement, i.e. ensuring that measured phosphorescence is from the applied phosphor and not from hot combustion gases.

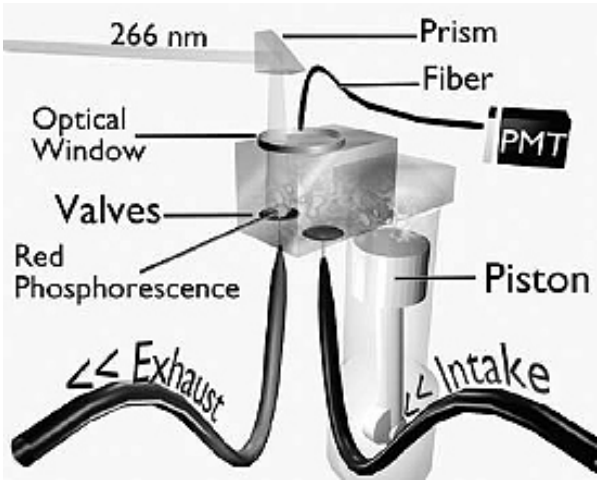

Figure 2.11. Optical modifications for phosphorescence measurement of valve temperature. Reprinted from [27].

Careful consideration must be given to the coating process by which the thermographic phosphor is applied. A thin layer is required such that the temperature of the phosphor accurately reflects the temperature of the piston. Should the phosphor layer be too thick, the measured temperatures will be artificially elevated as well as exhibit more transient behavior, as seen in the results of Särner *et. al.* [31]. From their results, the measured

phosphor temperatures vary by approximately 100 °C in 20 ms (180 CAD @ 1200 RPM) and were incorrectly identified as actual piston temperature fluctuations. Even with thin coatings, deposited soot particles affect the phosphor temperature, which affects the measured lifetime and temperature. Changes in the soot later thickness can be determined by the difference between the speed of soot deposition and oxidation. However, under steady engine operating conditions, these changes are very small.

3 Research Engine Methods and Equipment

3.1 Experimental Methodology

This chapter introduces the equipment, sensors, and instruments used to develop and conduct experiments to measure piston temperature. The embedding required a number of modifications to be made to the stock piston and engine block. Changes to the engine itself were performed by Ward [24] and were used in this research.

3.2 Engine Description

The engine investigated was a Briggs & Stratton INTEK model 110602 type 0015. It was an air-cooled, single cylinder, four-stroke, vertical shaft engine with overhead valves. The air cooling is accomplished by vanes cast into the engine flywheel and directed by the engine cover. The production ignition system for the INTEK engine utilizes impregnated magnets in the flywheel to achieve ignition at 19 degrees before top dead center (°BTDC). Specifications for the engine are listed in Table 3.1.

Bore	68.27 mm
Stroke	45.72 mm
Displacement	167.4 cm^3
Connecting Rod Length	88.57 mm
Compression Ratio	6.6:1
Wrist Pin Offset	0.381 mm

Table 3.1. INTEK Model 110602 engine specifications

3.3 Engine Modifications for Optical Access

3.3.1 Block Modifications

Modifications were made to the stock engine block and piston to allow optical access. For optical access to the engine cylinder, two through holes were drilled into the block normal to the cylinder bore, and perpendicular to the wrist pin axis. The holes were located a distance of 46.032 mm below the deck surface and directly across the bore from each other. The hole on the exhaust side of the block passed through the pushrod cavity. For this research, the intake (or thrust) side of the block was the input, or pitching, side and the exhaust (or anti-thrust) side of the block was the collection side.

Sealing of the combustion chamber was accomplished through the use of sapphire windows on both the pitching side and the collection side. The windows were kept as small as possible while still allowing adjustments in alignment to be made to the optical system. As a result, the windows used were 9.525 mm in diameter and 0.508 mm thick. Two window holders were designed and fabricated out of Invar 36 to hold and accurately position the windows against the cylinder bore. Two 12.70 mm holes were counterbored into the engine block concentric to the optical access ports. The holes were bored to a depth such that there was 0.051 mm of the engine block remaining between the cylinder bore and the bottom of the holes. A ceramic adhesive (Cotronics Resbond 940) was used to attach the windows to the window holders and further minimize the clearance between the cylinder and the window face. Viton O-rings were used to seal the combustion chamber at the window locations, as well as to seal the hole through the pushrod cavity.

3.3.2 Piston Modifications

In order to embed the fiber Bragg grating sensor in the piston a channel was machined into the crown surface. The channel is located along a diameter perpendicular to the wrist pin axis, across the center of the piston and in the same orientation as the optical access holes. Figure 3.1 shows the piston design from different angles, illustrating the orientation of the channel in relation to the wrist pin axis and the methods used for alignment. Two bosses were left within the groove to more accurately locate the FBG sensor. Each boss was located 5.874 mm from the piston edge and had a 0.508 mm hole drilled through it to hold the FBG.

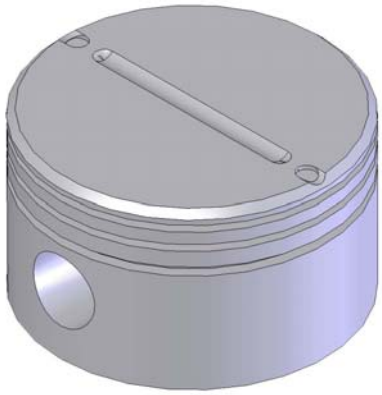

Figure 3.1. Engine piston design for embedding FBG temperature sensor

After machining, the optical fiber with the FBG sensor was placed into a piece of stainless steel tubing for protection as well as to help isolate the sensor from any strain effects. The stainless steel tube was then inserted into the piston channel, passing through the holes in the two bosses. The tube was not allowed to extend entirely to the piston edge on the input side, creating a small area between the boss and piston edge for an epoxy to be

applied to the exposed optical fiber to attach it to the piston. The picture in Figure 3.2 illustrates the alignment and orientation of the tube and fiber in the piston groove on the input side of the piston.

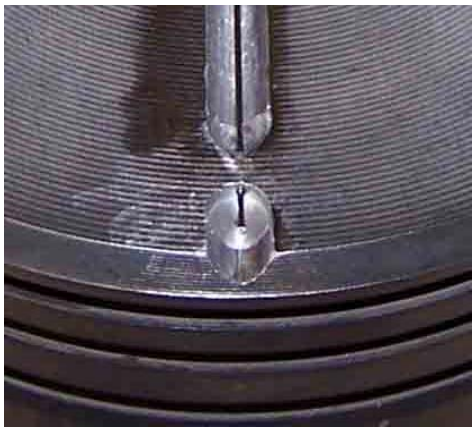

Figure 3.2. B&S INTEK piston showing inserted SS tube and location where FBG will be attached.

Two different embedding processes were used to fill the piston channel and secure the optical fiber. The first method involved filling the groove that had the tube in it with JB Weld and then filling the small remaining groove and exposed fiber with epoxy. The piston crown surface was then sanded progressively with 400, 600, 800, and 1200 grit sandpaper down to an even surface. The ends of the embedded optical fiber were further polished with a solution of colloidal alumina on a 1 μm polishing cloth, both from Lapmaster. This piston was used in preliminary engine tests to optimize alignment and to take data for engine motoring conditions.

The second method of sensor embedding involved an electroplating process. Instead of using JB Weld to fill the groove, an electroplating process was used to deposit nickel into the groove. Electroplating was chosen both due to the high strength of the deposited material

and the thermal conductivity of the resulting metal. It also has the advantage of being a low temperature process, which minimizes the possibility of damaging the embedded sensor. A full description of the electroplating process, including a number of steps to prepare the piston, is given by Ward [24].

3.4 Engine Test Cell

Engine tests were performed on a vertical shaft dynamometer to maintain constant engine speeds. This 10 hp model 83274 AC dynamometer was made by the Cox Instruments Division of the Lynel Corporation, and was donated to the ERC by Briggs & Stratton. The engine was coupled to the dynamometer by a Morflex 802 coupling.

Torque measurements were made using a load cell attached to the dynamometer. This sensor measured stress in the solid metal link that connected the free-floating dynamometer to a stationary ground via a 0.3 m moment arm. This device was able to measure both positive and negative loads [33].

An optical shaft encoder from BEI Motion Systems was used to determine the angular crankshaft position. A divider was used to reduce the resolution of the encoder from $1/6^{th}$ of a crank angle to ½ of a crank angle, reducing the amount of required memory. The outputs from the encoder provided two pulses per graduation (A and B pulses) in addition to one pulse per revolution (Z pulse). A Newport P600A tachometer counted Z pulses to determine engine speed.

Cylinder pressure was measured using a Kistler model 6061 piezoelectric pressure transducer located in the engine head. This sensor was designed specifically for combustion

engine applications where high frequency, time-resolved pressure measurements are necessary to allow accurate calculation of engine power and IMEP.

The pressure data were recorded using a Hi-Techniques HT-600 data acquisition system. Since the Z pulse from the shaft encoder is given each revolution, which is twice for each 4-stroke engine cycle, an optical switch was included in the system to trigger the data acquisition system every other revolution at top dead center of the compression stroke. Pressure data were then recorded at each A pulse from the shaft encoder.

All engine tests were conducted using EPA Tier II EEE fuel supplied by Haltermann Products. The fuel specifications are listed in Table 3.2.

Test	Units	Result
Specific Gravity	kg/L	0.741
Olefins	% Volume	0.4
Aromatics	% Volume	27.5
Saturates	% Volume	72.1
Research Octane # (RON)		97.0
Motor Octane # (MON)		88.0
Octane Number (RON + MON) / 2		92.5
Octane Sensitivity		9.0
Net Heating Value (LHV)	MJ/kg	43.0

Table 3.2. Fuel properties for EPA Tier II EEE from Haltermann Products

Engine temperatures were made to evaluate performance and to provide a means for determining the steady-state operating conditions of each test condition. Thermocouples were placed in the oil sump in the crankcase and in the exhaust manifold.

Further specifications for the equipment used in the engine test environment are provided in the Master's thesis by Albert [34].

3.5 Fiber Bragg Grating

The fiber Bragg gratings used for the piston temperature measurements were manufactured and prepared by O/E Land Inc. A small length of the polyimide buffer was removed from each fiber to produce the Bragg grating. Once written, the grating area of the fiber was recoated with a thin layer of polyimide for protection and reinforcement.

With the FBG securely embedded in the engine piston, a set of calibration measurements was taken to determine the Bragg wavelength shift versus piston temperature. Using a laboratory oven with the VCSEL diode, a ThorLabs PDA255 photodetector and digital oscilloscope, FBG transmitted power measurements were taken for oven temperatures from 24 to 60 °C. The PDA255 detector had its protective window removed, eliminating a high-magnitude etalon formed between the detector array and the window. The experimental piston was fastened to an optical breadboard along with the pitching and collection optics and the system was aligned for maximum light transmission. Temperature readings were recorded from two K-type thermocouples. One thermocouple was in contact with the center of the piston crown, while the other was allowed to extend into the air above the piston to gauge the air temperature inside the oven. The thermocouple temperatures were measured with a Fluke 50D K/J Thermometer.

The measured power transmission through the embedded FBG for each piston temperature was plotted versus the correlated VCSEL wavelength, which are included in Appendix B.2. The resulting calculations of the Bragg wavelength were then plotted versus the measured piston temperature and a linear fit was applied to the data. A FBG sensitivity

of 81.6 ± 6.29 °C / nm was calculated and is shown below in Figure 3.3. The equation for the line of best linear fit is:

$$T = 81.625 \cdot \lambda_B - 1.2576e5 \qquad (3.1)$$

where λ_B is the measured Bragg wavelength in nm and T is the piston temperature in °C.

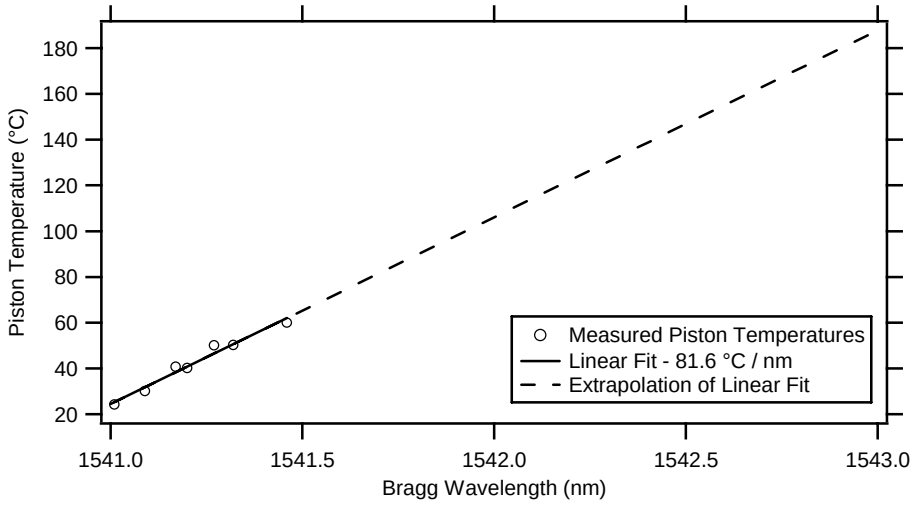

Figure 3.3. Piston-embedded FBG calibration, showing line of best linear fit

3.6 VCSEL Laser Diode

In order to interrogate the fiber Bragg grating, a wavelength-agile light source was required. This was found necessary [24] because of the high cycle-to-cycle variation of the light transmission through the piston. A light source capable of scanning the entire wavelength region of interest in a single engine cycle compensates for the differences in light variation cycle-to-cycle.

VCSEL stands for Vertical Cavity Surface-Emitting Laser. These small diodes are temperature controlled through a thermoelectric cooler (TEC) and the wavelength generated is proportional to the VCSEL diode current and temperature. These diodes can either be operated at a constant current or at a modulated current driven by a function generator. The Vertilas VCSEL diode (Thorlabs VCT1550, Serial number XCFR-RCCA-HQVS-X) and VCSEL diode driver (Thorlabs VITC002) used in this research allowed for operation of the diode from 0 °C to 50 °C and for currents from 1.5 mA to 12.5 mA.

For use in the engine optical assembly, a scanning speed of at least 30 kHz is required to obtain enough complete wavelength scans at BDC, when the embedded Bragg grating is aligned with the rest of the engine optics. To provide this modulation, a 30 MHz function generator was used (Stanford Research Systems, Model DS345). A 10 pin connector on the VCSEL control board provided a means for monitoring the set and actual TEC Thermistor resistance as well as the set and actual diode current. A pinout for this connector is described below in Table 3.3.

PIN	Signal	Range
1	GND	
2	LD ON	TTL, High when the laser output is switched on
3	ERROR	TTL, High when an error occurs
4	ILD SET	Set laser current, 100 mV / mA
5	ILD ACT	Actual laser current, 100 mV / mA
6	IPD	Photodiode current, 1 V / mA
7	R ACT	Actual Thermistor resistance, 100 mV / kΩ
8	R SET	Set Thermistor resistance, 100 mV / kΩ
9	OUT OF WIN	TTL, High when the resistance is out of the window
10	TEC ON	TTL, High when the temperature control is switched on

Table 3.3. Description of the 10 pin connector MEASURE (CON5) for VCSEL driver

Three small potentiometers on the VCSEL driver board provided the means to adjust the diode current limit, diode set current, and the Thermistor set resistance. The Steinhart-Hart equation and coefficients for computing the actual diode temperature from the measured resistance are shown in (3.2) and Table 3.4.

$$\frac{1}{T} = A + B \cdot \ln(R) + C \cdot \ln(R)^3 \qquad (3.2)$$

T = Temperature in K

R = Thermistor resistance in Ω

A	1.129148E-03
B	2.341250E-04
C	8.76741E-08

Table 3.4. Steinhart-Hart coefficients for VCSEL TEC Thermistor

4 Optical System Analysis

This chapter begins with a presentation of the optical system developed by Ward [24], including the primary difficulties in operating that system. Thorough analysis of the optical system and relevant optical phenomena will be presented, the outcome of which are modifications to the optical system and an improved experimental technique. In addition, an analysis of the VCSEL operating behavior is presented along with a method to calibrate and measure the actual time-varying VCSEL wavelength.

4.1 Original Engine Optical System Design

The optical system used for this research was based on the system developed by Ward [24]. The FBG sensor used was first stripped of its polymer buffer and then sputtered with thin layers of titanium and nickel, approximately 50 nm and 100 nm thick, respectively. By sputtering the fiber with metal, the sensor was able to be embedded into the metallic structure of the engine piston through an electroplating process. The prepared FBG was then inserted into a stainless steel tube and guided into a channel on the surface of the engine piston using two alignment bosses, as shown previously in Figures 3.1, 3.2 and 3.3. A small section of the metal sputtered FBG was allowed to stick out from the tube to ensure that there was proper bonding between the sensor and the piston. A detailed electroplating process was used to firmly hold both the FBG and the stainless steel tube and to completely fill the groove.

Once embedded, motoring and firing optical traces were obtained by using a fast scanning laser, photodetector and oscilloscope. These traces, shown below in Figure 4.1,

identify the center wavelength of the embedded FBG for stationary, motoring, and firing cases.

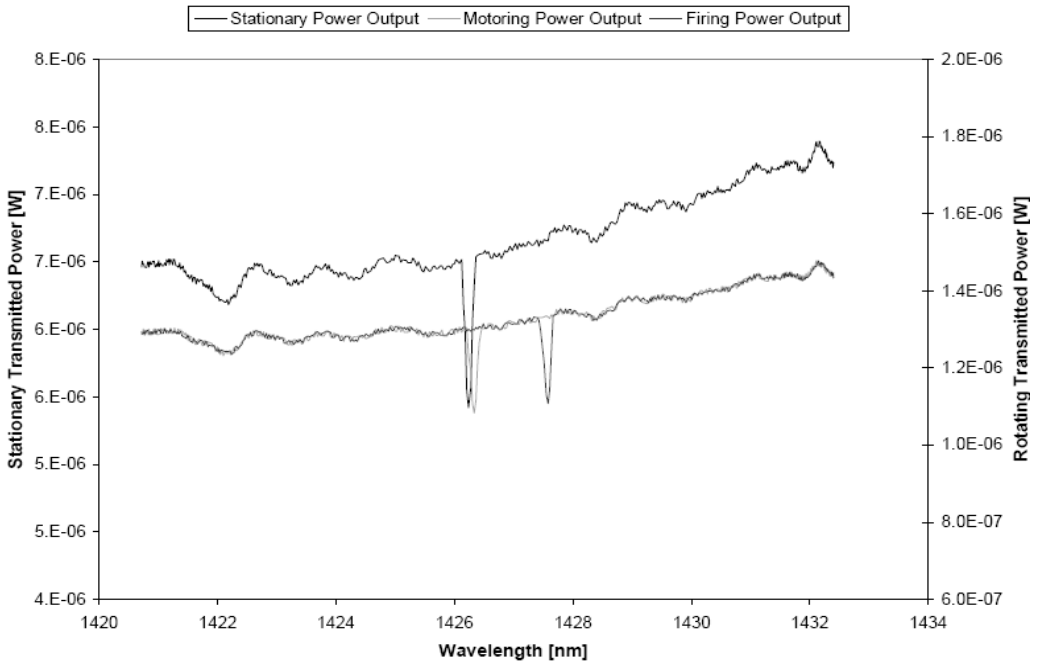

Figure 4.1. Transmitted power traces for stationary and rotating engine conditions displaying the shift in center wavelength of the embedded FBG.

The data in this figure reveal significant transmission losses of the coupled laser light, as can be seen by the relatively small dips caused by the embedded FBG. At the center wavelength, the attenuation is approximately 15%, or -0.7 dB, and took considerable time and alignment to obtain. While the Bragg dips in this trace are easily seen, there is a large discrepancy between these measurements and an ideal Bragg profile, as shown in Figure 4.2. Here, the attenuation caused by the Bragg grating is significantly greater, measuring -23 dB or >99%. While it may not be possible to attain this attenuation during engine operation, investigations into the nature of light transmission and coupling between fibers were made to understand possible areas for improvement.

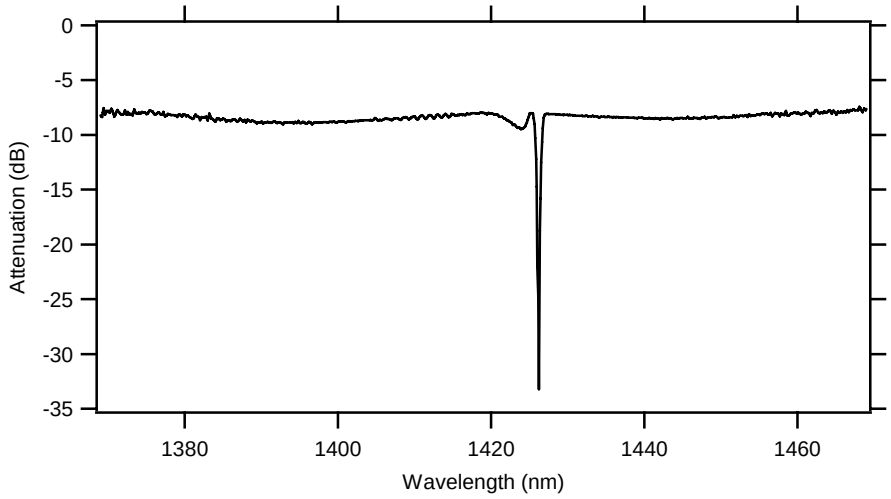

Figure 4.2. Ideal attenuation through FBG, measured with SLED and OSA

4.2 Fiber Coating and Embedding

A thorough analysis of optical transmission through fibers with various buffers and embedded by several different techniques was conducted.

4.2.1 Buffer Effects on Transmission

Optical fibers rely on concentric layers of different refractive index to maintain high transmission and high signal-to-noise ratios. While both the core and cladding of an optical fiber are made of glass (silica), the buffer is typically a polymer, such as acrylate. The role of the buffer is to remove light traveling in the cladding through absorption and dispersion, which happens at the cladding-buffer interface.

For embedding into the engine piston, it was necessary to remove this buffer, since the polymer material is incapable of operating at engine temperatures. To understand the effect of buffer removal, an experiment was designed to profile the transmission through

optical fibers. Each optical fiber under consideration was mounted on an optical platform and aligned with a photodetector on one side. The other side of the experimental fiber was aligned with a connectorized fiber held in a XYZ translation stage. A representation of this setup is shown below in Figure 4.3. Adjustments were then made to align and center the two fibers. Once aligned, the fiber held in the XYZ stage was traversed and the measured transmitted power yielded transmission profiles of power versus transverse displacement from center.

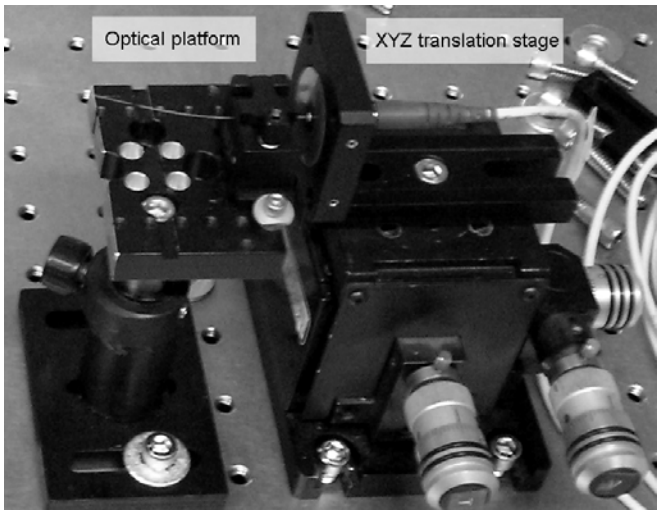

Figure 4.3. Optical platform and XYZ translation stage for transverse displacement measurements

Both buffered and unbuffered 9 μm, single mode fibers were tested using this setup and the results from these scans are shown in Figure 4.4. The profile for the fiber with its buffer intact is narrow – all of the transmitted power is within a region of approximately 9 μm. This profile corresponds to light transmission in the core mode of the optical fiber only, since any light traveling in the cladding of the fiber was attenuated by the buffer. The profiles for the fibers with their buffers removed are significantly wider. Without the

attenuation by the buffer, light travels through the cladding as well as the core, leading to a broader transmission region of 80 – 100 μm. These effects are known as cladding modes.

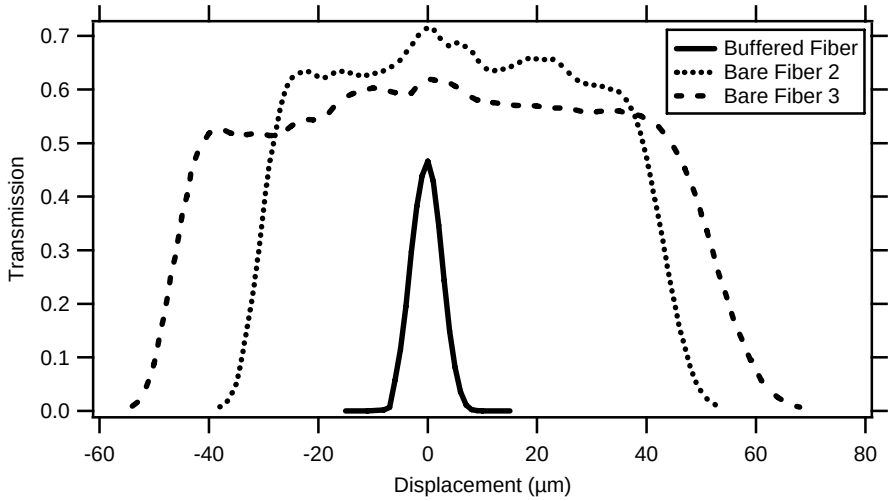

Figure 4.4. Transmission profiles for 10 cm long, 9 μm optical fiber with and without polymer buffer

The broader transmission region caused by the buffer removal makes detection of the Bragg wavelength considerably more difficult. While light traveling through the cladding experienced some attenuation from the Bragg grating, the attenuation was not as great as that experienced by light traveling through the fiber core. As a result, light transmitted entirely through the cladding decreased the depth of a dip at the Bragg wavelength. Thus, methods were sought to eliminate these cladding modes and increase the depth caused by the FBG at the Bragg wavelength.

4.2.2 Alternative Embedding Techniques

The fiber embedding process provides an opportunity to explore alternative adhesives and attachment techniques to hold the FBG sensor to the piston. There are a number of light absorbing epoxies available with favorable specifications capable of withstanding engine piston temperatures. Selection of an appropriate epoxy entailed similar transverse profile measurements for a variety of adhesives. A list of the epoxies tested is shown below in Table 4.1.

Epoxies Considered:	FIS Blue Dye	EpoTek 320	EpoTek 353ND Black
Glass Transition Temp. (Tg)	95 °C	> 70 °C	≥ 90 °C
Operating Temp.	-60 °C to 100 °C	N/A	-55 °C to 225 °C
Index of Refraction	N/A	1.5265	N/A
Spectral Transmission	97%	<0.0001%	< 3% @ 1550 nm

Table 4.1. Investigated epoxies for embedding and light absorption

Similar transverse transmission experiments were performed for each of these epoxies to quantify the amount of cladding mode absorbance. As shown in Figure 4.5 below, each of the epoxies do a reasonable job of suppressing cladding modes and narrowing the transmission profiles. However, the sample with EpoTek 353ND Black has higher transmission at the center of its profile, which is the location of the desired core mode. While the cladding modes are not completely eliminated, they are noticeably attenuated. With an operating temperature range up to 225 °C, the 353ND Black is well suited for use in an engine piston. Using this epoxy to install and firmly hold the FBG in the piston will result in more noticeable Bragg dips and a strong, reliable bond.

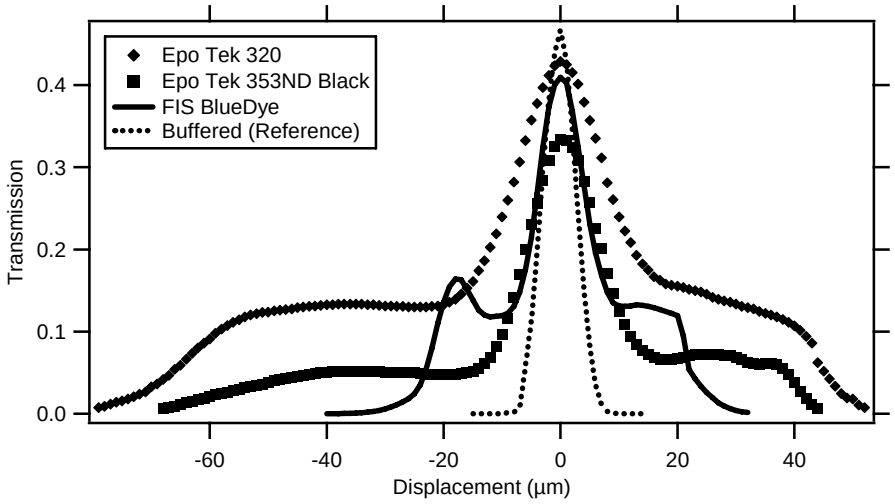

Figure 4.5. Transmission profiles for 10 cm long, 9 μm optical fiber embedded in 3 cm of optically absorptive epoxies

4.3 Dual Clad Interrogation Method

While the current implementation of the FBG sensor in the engine piston relies on the measurement of transmitted light, it is also possible to measure the light reflected from the FBG to determine the Bragg wavelength and from that the temperature. As introduced in Chapter 2, the wavelengths that are filtered by the FBG appear as a dip in a transmission plot, but occur also as peaks in the reflected measurements. A method utilizing dual clad fiber makes such a measurement possible

Dual clad fiber resembles regular single mode fiber, with the addition of another layer of silica before the buffer layer. Thus, there are two silica-silica interfaces that create two separate waveguides for light, as can be seen below in Figure 4.6. If broadband light is transmitted through the core of the dual clad fiber and coupled into an FBG, the reflected light can then be coupled back through the first cladding, allowing measurement of the Bragg

wavelength. A dual clad fiber setup was developed by Chris Hagen and Jason Schmidt at the University of Wisconsin – Madison, making it possible to obtain these measurements.

Figure 4.6. Detailed enlargement of dual clad fiber end

Using a similar experimental optical setup, measurements were taken to determine the susceptibility of such a system to misalignment. With a pitching gap of approximately 0.004", the measured Bragg height was 7.21 dB, as shown in Figure 4.7 below. These results compare favorably with measurements taken in transmission for a pitching gap of 0.029". However, when the dual clad method is used for a 0.029" pitching gap the Bragg peak drops to 4.08 dB, nearly an order of magnitude smaller than the 30 dB dip seen in transmission.

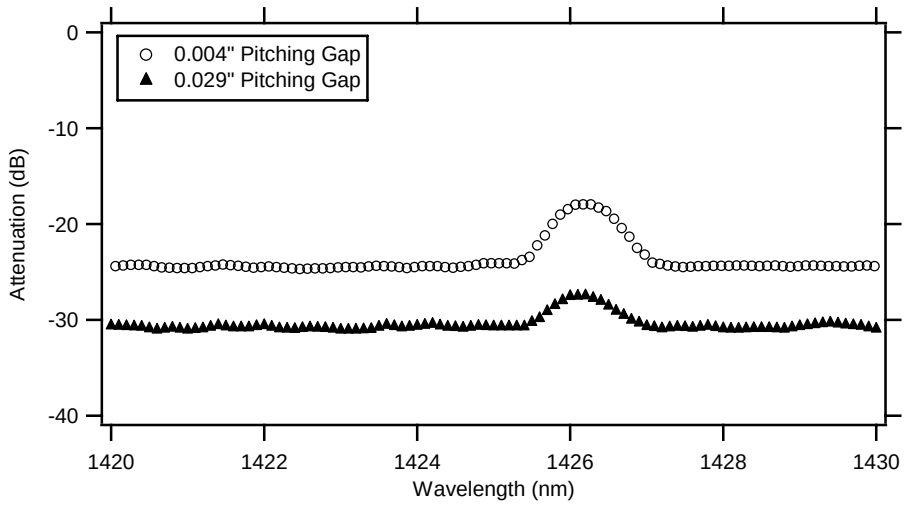

Figure 4.7. Bragg center wavelengths revealing decrease in Bragg height with increasing pitching gap distance

Performing a series of similar measurements resulted in the transverse transmission profiles shown in Figure 4.8. The Bragg heights shown here were considerably smaller than the corresponding Bragg dips measured in transmission, which were on the order of -20 dB.

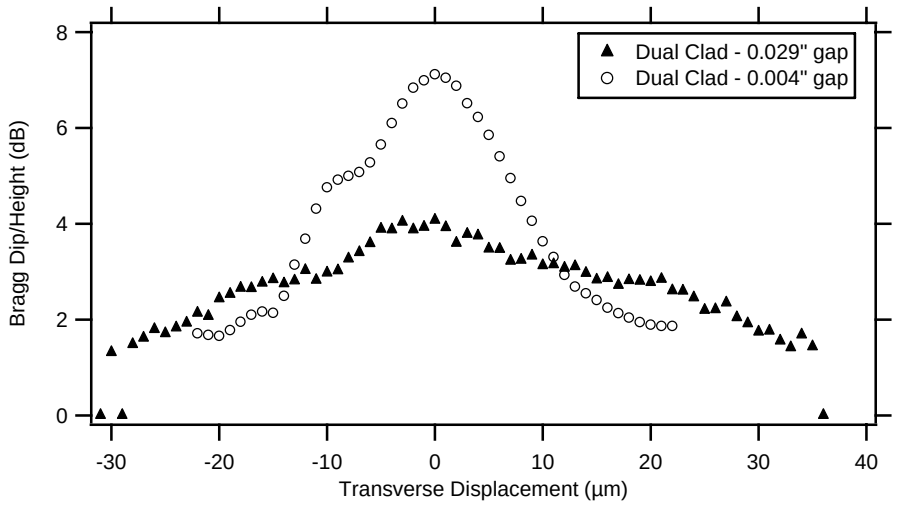

Figure 4.8. Bragg depths/heights for normal and dual clad interrogation methods

4.4 Misalignment Effects

The amount of attenuation caused by a Bragg grating depends largely on wavelength and has also been shown to depend on alignment as well. As two fibers are misaligned, the area of intersection of their transmission cones decreases. When the collection fiber becomes misaligned, the amount of light transmitted decreases. These effects were examined for fully buffered fibers as well as for polyimide buffered fiber.

4.4.1 Acrylate Buffered Fiber

Using the same optical setup as mentioned previously, a sample length of acrylate-buffered fiber was examined. As the collection fiber was moved across the axis of transmission, measurements were taken with a SLED and OSA. The data collected were then analyzed by a user function written in IGOR (Appendix A.1). Experiments were conducted for separation distances of 0.004" and 0.029". The results of these analyses were transmission profiles displaying Bragg depths versus displacement, as shown in Figure 4.9.

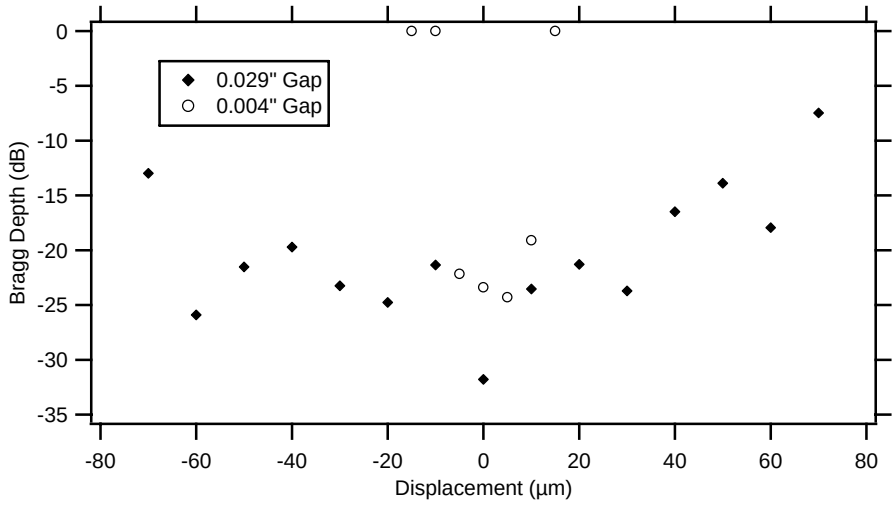

Figure 4.9. Bragg depths for normally dispersive light measured in transmission

From previous experiments, it was concluded that removing the acrylate buffer caused a significant increase in cladding mode propagation. To minimize these cladding modes, a polyimide buffer material was investigated. Polyimide has the added benefit over normal acrylate buffers of being able to withstand much higher temperature climates (up to 300 °C). In addition to cladding mode attenuation, retaining the buffer increases fiber structural integrity. In order to determine the effects of using polyimide as a buffer, a FBG written on polyimide-buffered fiber was obtained.

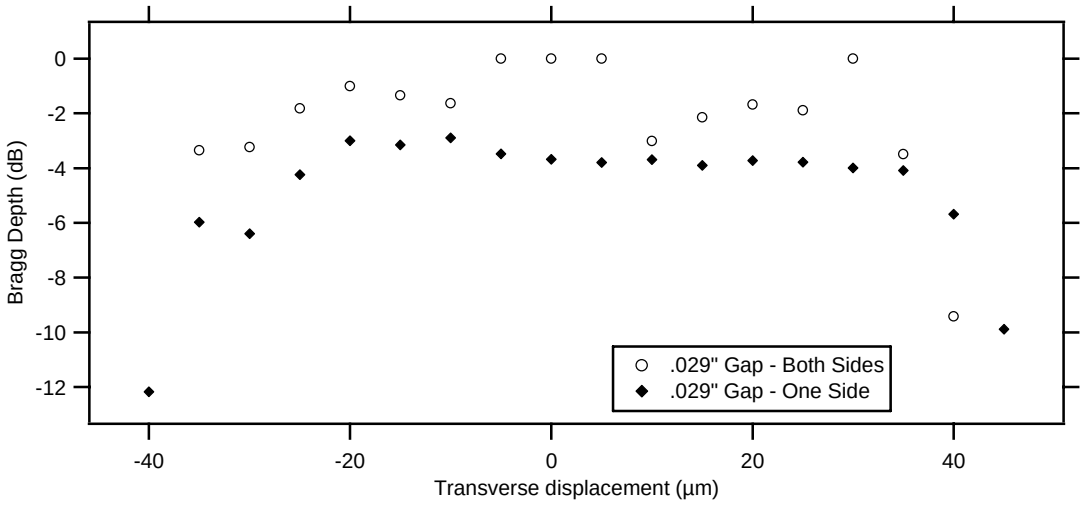

Figure 4.10. Bragg depths as measured in transmission through a polyimide buffered FBG

4.4.2 Polyimide Buffered FBG

Performing transverse Bragg dip measurements on the polyimide FBG resulted in the data shown in Figure 4.10. While the Bragg center wavelength is observable over a region of approximately 80 µm, when the pitching fiber and the FBG are perfectly aligned, the transmission profiles become difficult to analyze. Instead of the expected Bragg dip caused

by the grating, there was a peak with a local maximum in the region of interest. A possible explanation for this phenomenon is that the wavelength reflected by the grating transmitted back into the gain medium of the SLED, causing significant amplification of the center wavelength. Incorporating an optical isolator into the pitching assembly would eliminate this problem. While these analyses have focused on the effects of alignment on Bragg grating attenuation, trends were observed that suggest the Bragg center wavelength also depends on alignment.

At constant temperature and strain, the Bragg center wavelength should remain constant. However, comparing these wavelengths as a function of alignment (transverse displacement) shows a strong linear trend. From Figure 4.11 below, it can be seen that as the transverse displacement between the two fibers increases, so does the measured Bragg center wavelength.

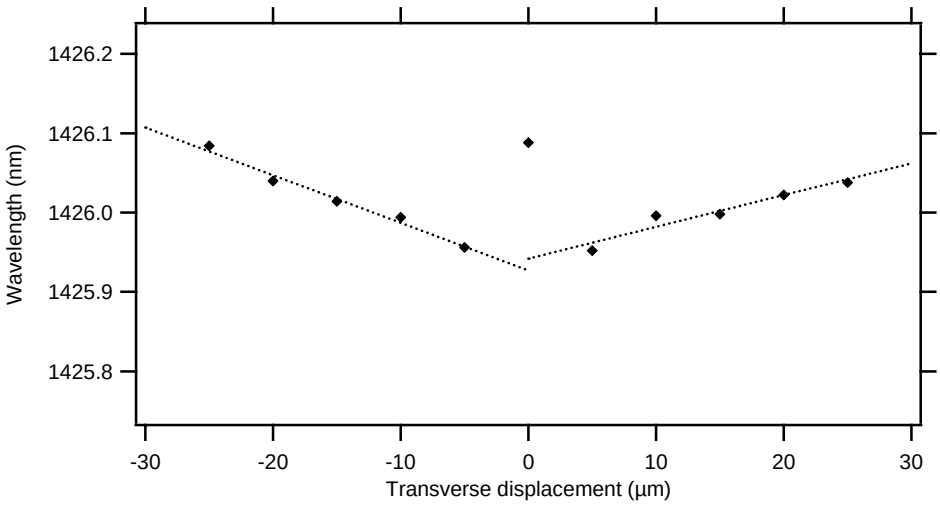

Figure 4.11. Bragg center wavelength measurements through polyimide buffered fiber

The analysis of these results required a thorough understanding of Bragg grating and Gaussian optical theory. As the two optical fibers were misaligned, light was coupled at an increasing angle. While this angle was within the acceptance cone for single mode fiber (called the numerical aperture or NA), light was traveling with a greater incidence angle. Thus, when this angled light passed through the FBG, it experienced a slightly greater path length between each plane in the grating. Since the center wavelength reflected by a FBG depends linearly on the distance that light travels between each successive grating plane, light traveling through the FBG at an angle will result in a higher measured Bragg center wavelength than that measured when parallel light is coupled into the fiber.

It is of great importance to reduce this effect since perfect alignment can not be realized in a continuously operating engine. The measurements mentioned above indicate an error of ±0.1 nm in the Bragg center wavelength, which correspond to an error of ~±10 °C, an unacceptable error. A solution is required which will create greater consistency in the incidence angles of the pitched light. This challenge is ideally suited to the use of an aspheric lens in the pitching assembly.

4.4.3 Gaussian Optics

Gaussian optical theory states that light traveling through a lens will never be perfectly focused (to a point) but will reach a point of maximum focus defined as the beam waist. This effect is shown below in Figure 4.12. At this location, there is no divergence and the rays of light are perfectly parallel. If an optical fiber is placed at this location, light coupled through the fiber will also be parallel and the dependence on the magnitude of misalignment will be minimal.

To determine the focal length *f* for the aspheric lens, it is necessary to solve a system of equations from Gaussian optics. The first equation (4.1) matches the beam waist at the lens and the second (4.2) conserves the complex radius through the lens:

$$\omega_1^{\,2}\left[1+\left(\frac{\lambda\cdot x_1}{\pi\cdot\omega_1^{\,2}}\right)^2\right]=\omega_{lens}^{\,2}(x_1)=\omega_{lens}^{\,2}(x_2)=\omega_2^{\,2}\left[1+\left(\frac{\lambda\cdot x_2}{\pi\cdot\omega_2^{\,2}}\right)^2\right] \quad (4.1)$$

$$\frac{1}{q_2}=\frac{1}{q_1}-\frac{1}{f} \quad (4.2)$$

where ω_1 is the beam waist at the fiber (9 μm), ω_2 is the desired beam waist (400 μm), ω_{lens} is the beam waist at the lens, λ is the operating wavelength, x_1 is the distance between the fiber and the lens, x_2 is the distance between the lens and the desired waist location, and the complex radii q_1 and q_2 are defined as below in (4.3) and (4.5):

$$q_1=\frac{1}{\dfrac{x_1}{x_1^{\,2}+x_{R,1}^{\,2}}-i\cdot\dfrac{\lambda}{\pi\cdot\omega_1^{\,2}}},\ x_{R,1}=\frac{\pi\omega_1^{\,2}}{\lambda} \quad (4.3, 4.4)$$

$$q_2=\frac{1}{\dfrac{x_2}{x_2^{\,2}+x_{R,2}^{\,2}}-i\cdot\dfrac{\lambda}{\pi\cdot\omega_2^{\,2}}},\ x_{R,2}=\frac{\pi\omega_2^{\,2}}{\lambda} \quad (4.5, 4.6)$$

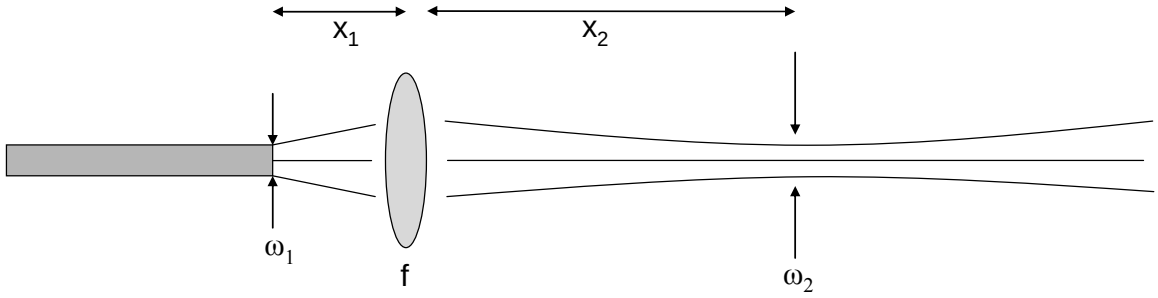

Figure 4.12. Schematic of Gaussian optical propagation through aspheric lens

Incorporating this theory into the engine optical system required selecting an aspheric lens capable of achieving a beam waist of 400 μm as well as reasonable distances for x_1 and x_2. Using a MATLAB program (Appendix A.3), it was determined that the A375TM-C lens from ThorLabs with a focal length of 7.5 mm was able to achieve a beam waist of 400 μm when the distances x_1 and x_2 are set as described in Table 4.2.

x_1	7.46 mm
x_2	69.61 mm

Table 4.2. Computed distances to incorporate aspheric lens into engine optical system

4.4.4 Improved Optical System Performance

Using a modified optical setup which included the aforementioned aspheric lens, several measurements were taken to confirm this approach. Locating the tip of the FBG fiber at the 400 um beam waist developed by the aspheric lens, transmission measurements were taken and compared to the results from experiments where there was no lens. Figure 4.13 below shows the corresponding Bragg depths for a number of measurements taken for incremental distances of transverse displacement.

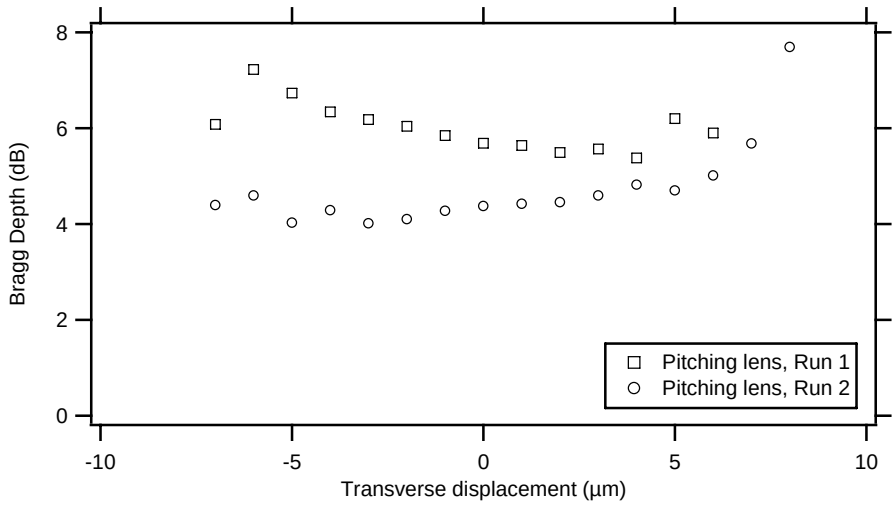

Figure 4.13. Measured Bragg depths using collimating aspheric lens

While it is necessary to quantify the Bragg dip depths through this modified system, the motivation for the modification were to minimize, if not eliminate, the wavelength shift caused by misalignment. Thus, the data were also analyzed to identify the Bragg center wavelength as a function of transverse displacement. Comparing these results with previously measured center wavelengths for the system without an aspheric lens shows a considerable improvement in center wavelength precision, where precision is defined as the uniformity of repeated measurements of a certain parameter. These results can be clearly seen graphically below in Figure 4.14.

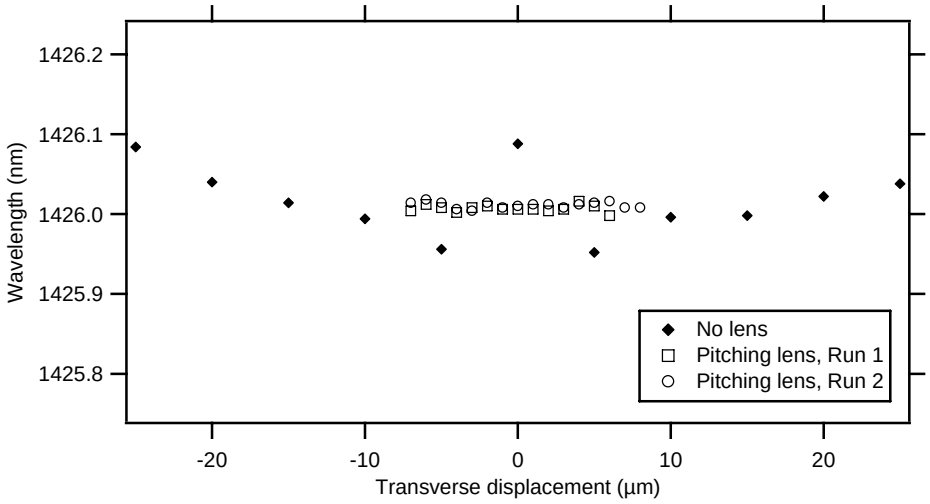

Figure 4.14. Measured Bragg center wavelengths using collimating lens

4.5 Continued Cladding Mode Investigation

As with many optical systems, the instruments and optical elements in this experimental design need to be aligned coaxially. However, such an alignment, when combined with a focused light source with a small divergence angle, can lead to light transmission in both of the silica waveguides in a fiber (core and cladding). This is due to the decreased number of instances of internal reflection, where propagating light contacts the core/cladding or cladding/buffer interface and is completely reflected back into the fiber. The purpose of the fiber optic buffer is, conversely, to significantly absorb all light propagating through the cladding. Investigating this issue resulted in the following experiment.

If the light incident on the FBG fiber tip was not coaxial, there would be an increase in the number of cladding/buffer contacts during light transmission. Since light transmission is still desired, the pitched light must remain within the acceptance angle of the fiber.

Consequently, the experimental setup was modified such that the pitched light was incident on the fiber at an angle equal to half the acceptance angle (~ 0.055 radians). Measurements were then taken for both the Bragg depth and center wavelength and compared to results from the non-angled experiment, shown below in Figure 4.15.

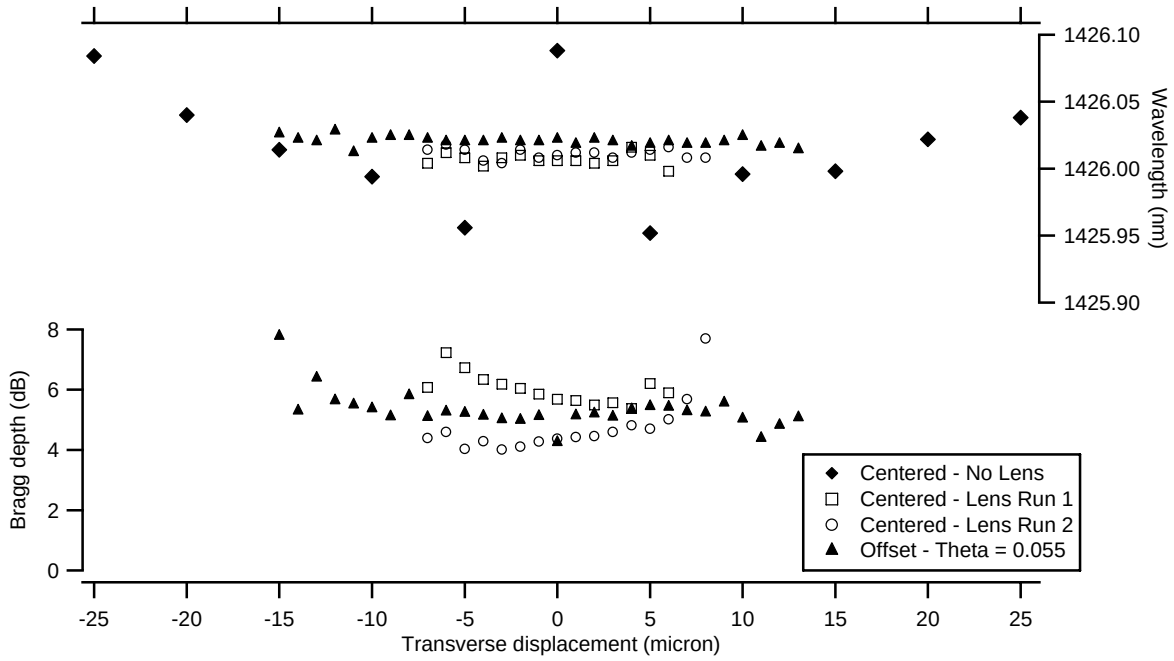

Figure 4.15. Measured Bragg center wavelengths and depths for offset pitching angle

The results from these offset pitching angle measurements reveal no significant improvement in the measured Bragg depth, and provide no greater consistency in the Bragg center wavelength than the case where the fibers are aligned.

4.6 VCSEL Calibration

As introduced in Chapter 3, the VCSEL diode is well suited for use as a wavelength scanning light source for this research. To incorporate the diode with the other optical elements of the system, a FC fiber pigtail was installed by OZ Optics. With this modification,

a series of measurements were performed to examine the operating wavelength of the diode for both constant current and modulated current modes.

4.6.1 Constant Current Mode

The VCSEL diode was operated in a constant current mode by using the controls available on the VCSEL control board from Thorlabs. As a precaution, the VCSEL current limit was set to 12.5 mA by connecting a multimeter to pin 4 and adjusting the LIMIT potentiometer P1 appropriately. To set the operating temperature and current of the diode, multimeters were connected to pins 5 and 7 while adjustments were made to the SET LASER and SET TEMP potentiometers P2 and P4. For the experiments performed, the diode was set to a temperature of 20 °C, unless noted.

To measure the wavelength of the VCSEL during operation, an Ando AQ-6315A optical spectrum analyzer (OSA) was used. The OSA uses an internal diffraction grating to measure power versus wavelength and saves this information to a simply formatted text file. Data reduction and manipulation were performed in a software package called IGOR, which is aptly suited to manipulating constant interval data, such as that from oscilloscopes and data acquisition systems.

Figure 4.16 below shows a series of measurements taken with the VCSEL in constant current mode. The location of maximum power in each profile was assigned to be the characteristic wavelength of the VCSEL at that particular current.

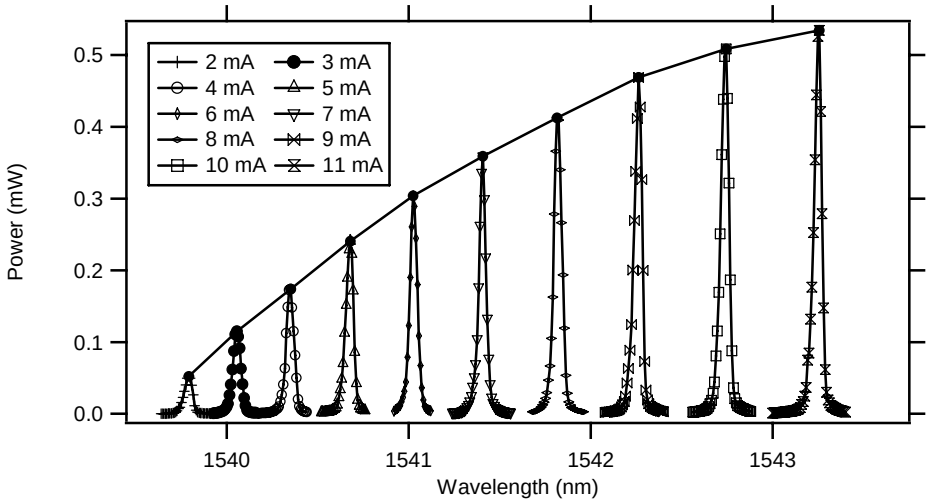

Figure 4.16. VCSEL profile for constant current mode at operating temperature of 20 °C

It is useful also to plot the location of peak power for each profile versus the VCSEL diode current. A power law equation of the form $\lambda = A_1 + A_2 \cdot I^{A_3}$ fits the data well and was used as a reference to determine the VCSEL wavelength during tests with the diode in modulated current mode. Figure 4.17 displays this wavelength profile and the coefficients for the power law fitting function.

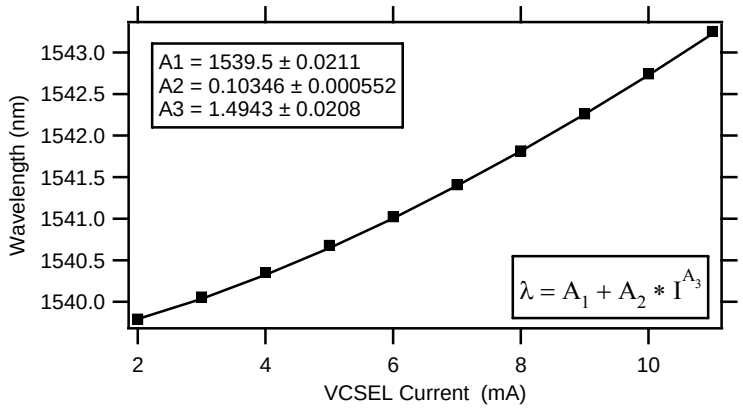

Figure 4.17. VCSEL diode wavelengths for constant current mode at operating temperature of 20 °C

4.6.2 Modulated Current Mode

The VCSEL diode can be operated in modulated current mode either by using the internal circuit on the VCSEL control board or by connecting an external function generator. Adjustment of the modulation frequency using the internal circuit involved a small potentiometer dial (P3) and required measurement on an oscilloscope to verify the actual frequency. Thus, it was beneficial to use an external function generator, where the frequency, amplitude and offset values can all be set accurately. The function generator was connected to the MOD EXT connector CON3 using a SMB to BNC cable. A triangular ramp function with an amplitude of 0.60 V and an offset of 0.30 V was used for all frequencies considered. Measurements were made with the PDA400 photodetector and a 350 MHz digital oscilloscope from Tektronix (Model TDS5032B).

Using the same optical setup, the first experiment was run with a modulation frequency of 1 kHz. Measurements were made of the actual VCSEL current and the power transmitted through the polyimide FBG. Using the provided conversion factor of 100 mV/mA, the VCSEL actual current was determined and plotted, shown below in Figure 4.18. The power measured by the photodetector was converted using the formula below (4.7) and was plotted to yield the data in Figure 4.19.

$$P_{photo\,\mathrm{det}\,ector} = \frac{V}{G * R} \quad (4.7)$$

V = Measured photodetector voltage

G = Transimpedence gain, 1.5 x 10^4 V/A

R = Responsivity, 0.9 A/W @ 1550 nm

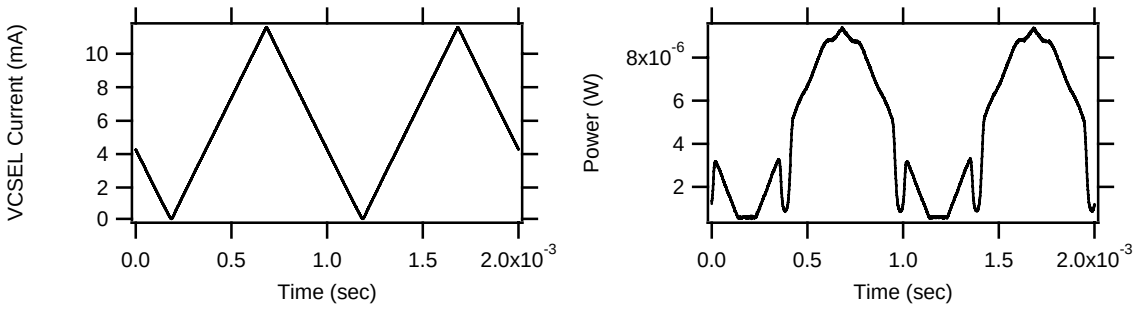

Figure 4.18 and Figure 4.19. Actual VCSEL current as measured from control board and measured power through polyimide FBG for modulation frequency of 1 kHz

The VCSEL current data were then converted to wavelength using the wavelength profile information represented by the data in Figure 4.17. By plotting the power data from the photodetector versus the correlated wavelength data from the VCSEL, the Bragg center wavelength was identified, shown below in Figure 4.20. There are two complete wavelength scans displayed in the figure, which correspond to the up-scan and down-scan of the VCSEL. The center wavelength identified by this method was 1540.6 nm, which agrees with the manufacturers specifications.

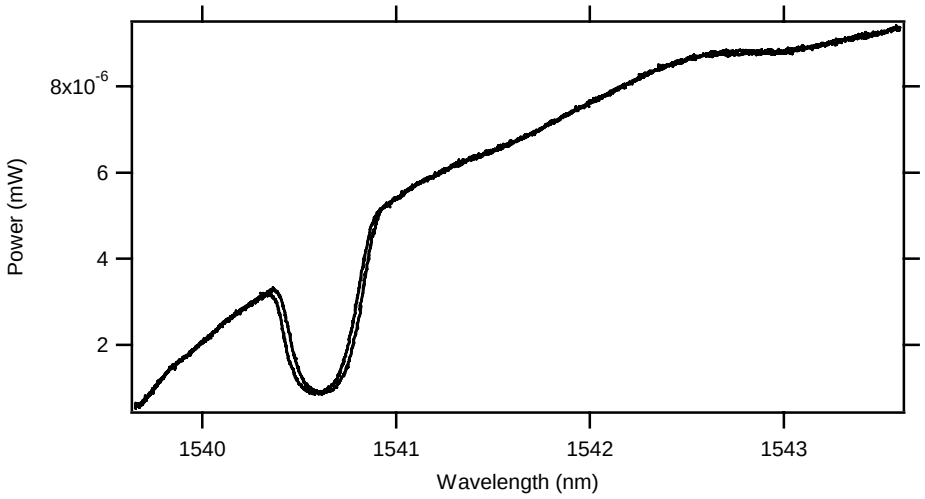

Figure 4.20. Measured power through FBG versus VCSEL wavelength correlated by actual current output from VCSEL control board for modulation frequency of 1 kHz

A faster scanning speed is required for engine measurements, due to the constraint of completing multiple wavelength traces during each coupling event at bottom dead center (BDC). As a result, a series of measurements were taken for frequencies ranging from 1 kHz to 100 kHz. The data from these measurements is provided in Appendix B.1.

As the scanning frequency was increased, an interesting phenomenon was observed. The actual VCSEL current and photodetector power data taken for a scanning speed of 100 kHz is presented below in Figures 4.21 and 4.22. Both traces display a rounding of the triangular ramp input function. In addition, the dips in the photodetector trace do not occur at symmetrical locations as they did for a scanning frequency of 1 kHz.

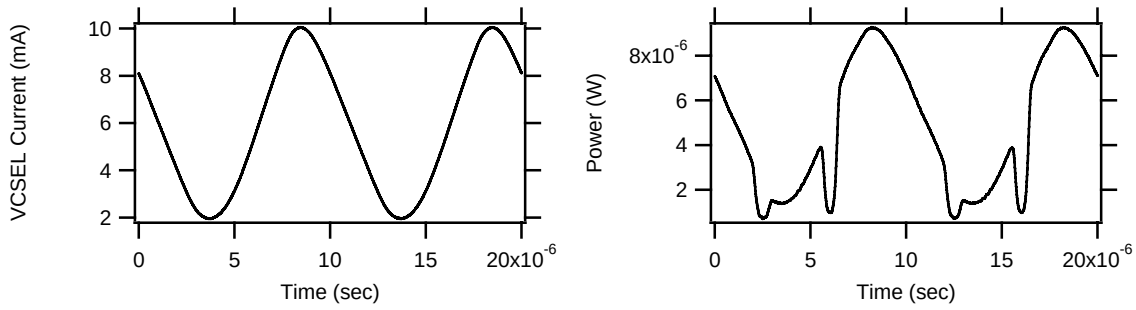

Figure 4.21 and Figure 4.22. Actual VCSEL current as measured from control board and measured power through polyimide FBG for modulation frequency of 100 kHz

Following the wavelength conversion procedure developed for the 1 kHz case, the plot of power versus wavelength was generated and is shown in Figure 4.23. The disparity between the up-scan and the down-scan becomes more apparent in this plot and indicates that the actual current output from the control board no longer predicts wavelength accurately.

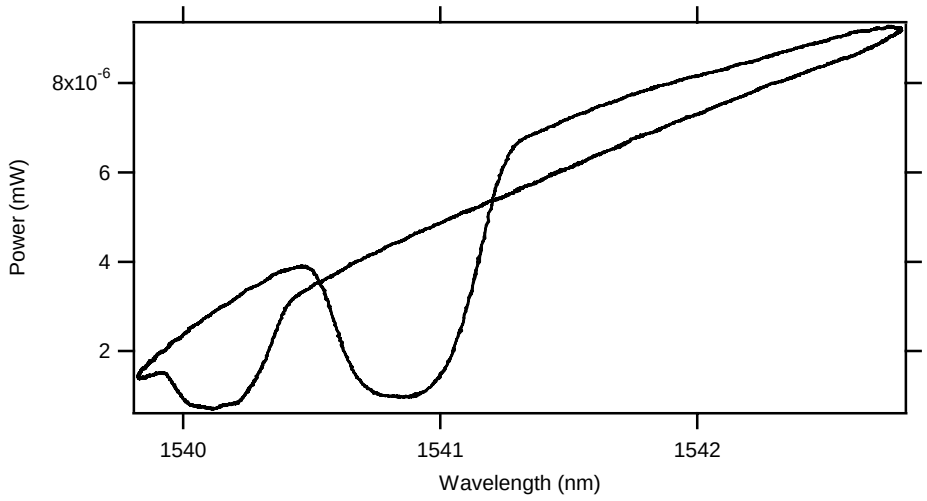

Figure 4.23. Measured power through FBG versus VCSEL wavelength correlated by actual current output from VCSEL control board for modulation frequency of 100 kHz

With the failure of the direct current to wavelength correlation, another means was necessary to determine the actual wavelength of the VCSEL diode as a function of time. To achieve this, a Mach-Zehnder etalon was used to monitor the VCSEL wavelength. A Mach-

Zehnder etalon is constructed using all fiber optic elements and a simplified diagram is shown below in Figure 4.24. Using a 50-50 beam splitter, the incoming light is evenly divided between two intermediate fibers that are of different lengths. When combined by another 50-50 beam splitter, the path length difference ΔL between the two fibers creates a unique interference pattern.

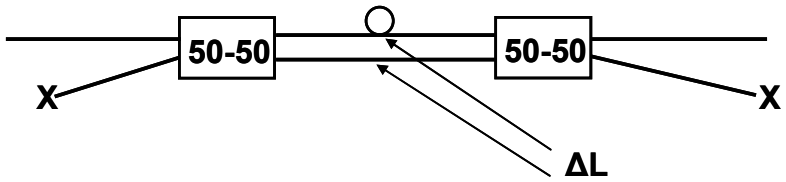

Figure 4.24. Diagram of Mach-Zehnder etalon

The free spectral range (FSR) of the etalon is defined as the distance between adjacent fringes and is inversely proportional to the path length difference ΔL of the Mach-Zehnder etalon. The fringes are an integer number of wavenumbers apart and provide a method for determining the relative wavelength at any point in time. A wavenumber is commonly measured in units of cm^{-1} and is inversely proportional to the absolute wavelength. The VCSEL profile is shown with the Mach-Zehnder etalon below in Figures 4.25 and 4.26.

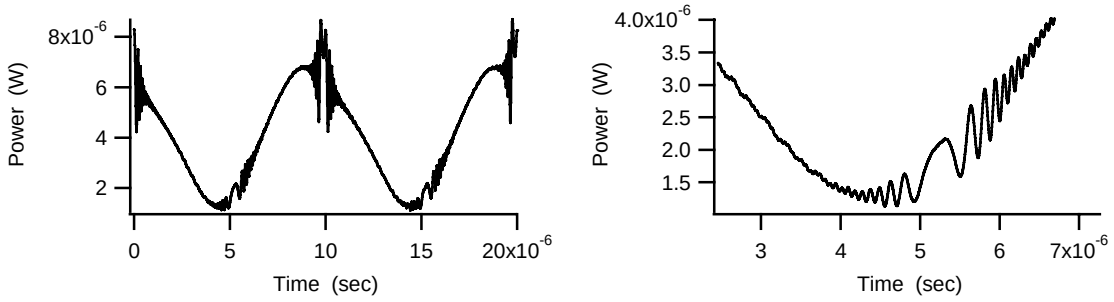

Figure 4.25 and Figure 4.26. VCSEL power showing fringes from Mach-Zehnder etalon

With an etalon used with a wavelength scanning source such as a VCSEL, the points in the scan where the spacing between the fringes is greatest corresponds to the points where the VCSEL wavelength is changing the slowest, i.e. at the points where the wavelength begins to scan in the opposite direction. From Figure 4.25 and 4.26, it can be seen that these points are not actually at the locations of lowest and highest power, but slightly later, which agrees with the delays seen in the Bragg peaks identified in the photodetector traces shown in Figure 4.22. Using this information, combined with the number of fringes between each reversal point, a correlation can be performed to determine the wavelength of the VCSEL as a function of time.

Since the information contained in the etalon can only give a relative definition of wavelength, an external reference is required to absolutely peg the wavelength at some specific point in the scan. An OSA trace was used to determine the limits of the wavelength scan, as shown below in Figure 4.27. These values were then correlated to the reversal points to generate an absolute wavelength reference for the VCSEL. A series of IGOR procedures was used to count the etalon fringes and correlate the VCSEL data to generate the absolute wavelength reference (Appendix A.2).

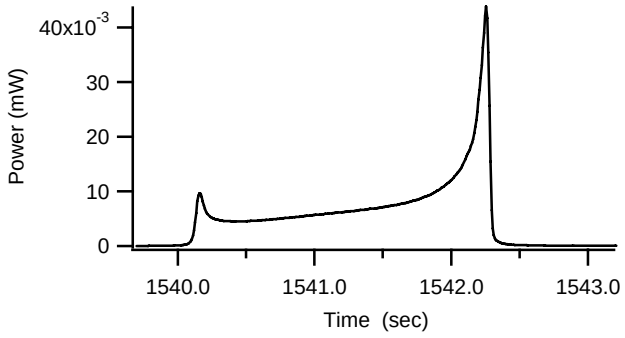

Figure 4.27. OSA Trace for VCSEL at scanning frequency of 100 kHz showing wavelength limits of scan range

Figure 4.28 below shows the number of etalon fringes counted by the IGOR procedure on a relative scale. Through the correlation with the OSA trace, Figure 4.29 displays the absolute wavelength of the VCSEL as a function of time.

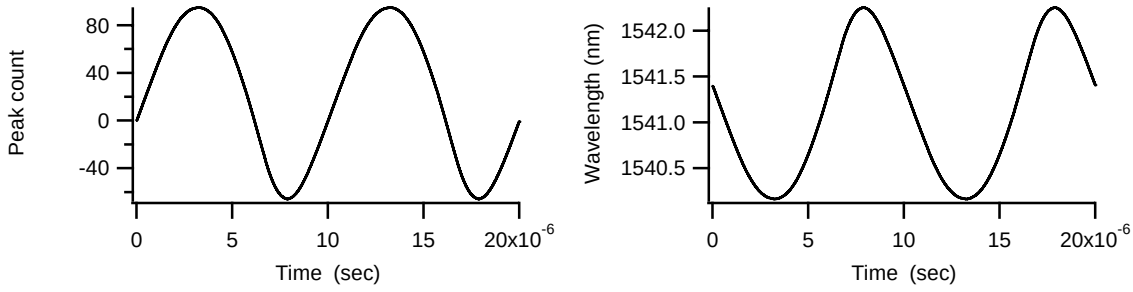

Figure 4.28 and Figure 4.29. Count of etalon fringes and correlated VCSEL wavelength versus time

Plotting the measured photodetector power (Figure 4.22) versus the correlated wavelength yields the Bragg dip plot shown in Figure 4.30. The trace contains ten complete scan cycles, which are seen to overlay each other exceptionally well. The two different Bragg depths are a result of the different locations of the Bragg dip on the up-scan and the down-scan.

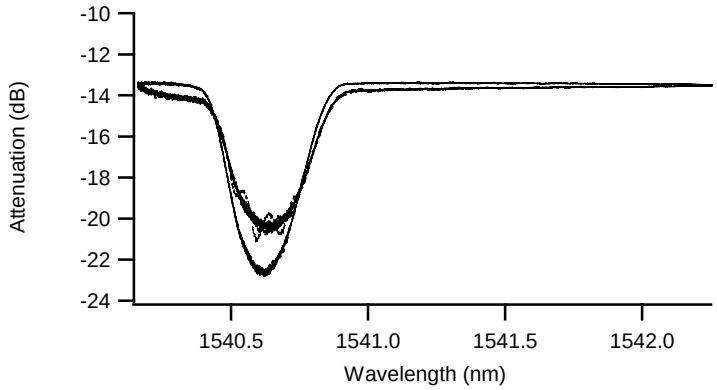

Figure 4.30. Calculated attenuation through FBG versus VCSEL wavelength correlated by Mach-Zehnder etalon for modulation frequency of 100 kHz

As a result of this analysis, it is possible to compute the absolute wavelength of the VCSEL in modulated current mode and to generate attenuation plots that accurately locate the Bragg center wavelength.

5 Piston Temperature Measurement

5.1 Initial Engine Motoring Measurement

Following calibration of the embedded FBG sensor, the optical Briggs engine was reassembled and installed on the laboratory dynamometer. The laboratory intake manifold was redirected by a 45° elbow to allow attachment of the pitching optics. The engine was rotated by hand to near-BDC and the pitching optics were adjusted to again obtain an optical trace showing the dip from the embedded FBG. Taking 1000 averages of the measured photodetector power yielded the trace shown in Figure 5.1, indicating a Bragg wavelength of 1541.09 nm. From Equation 3.1, this wavelength corresponds to a piston temperature of 31.5 °C.

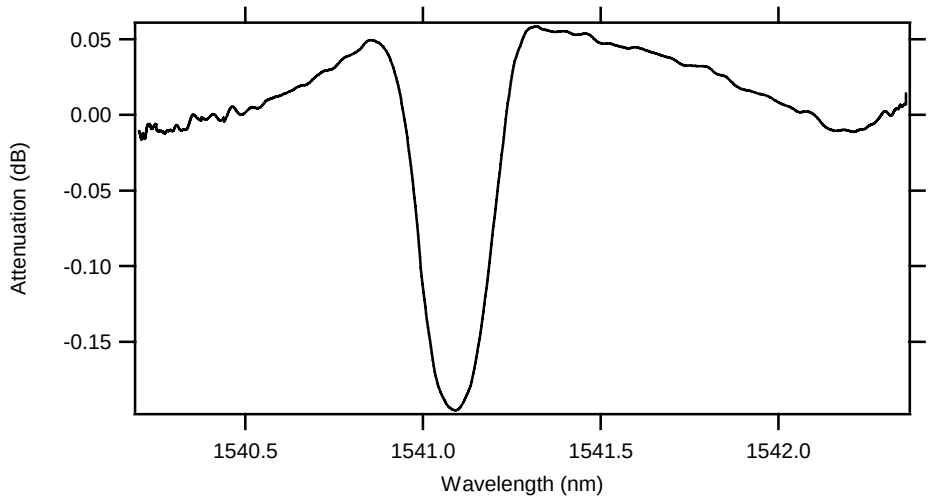

Figure 5.1. Transmitted VCSEL power for stationary engine with Bragg wavelength of 1541.09 nm

The engine was then motored at 600 RPM to properly calibrate the MotoTron timing system. After approximately 45 seconds, an audible metallic chirping was heard and the engine was immediately shut down. Once stopped, the engine was unable to be turned over by hand, which made removing the engine from the dynamometer and disassembling it more difficult. There were signs of severe scoring on both the cylinder and the piston, causing critical damage to the engine. Figures 5.2 and 5.3 show the extent of damage caused.

Figure 5.2 and Figure 5.3. Resulting damage from nickel deposit to cylinder and piston

Removing the piston from the engine cylinder required firm pounding by a hammer. Once removed, a small piece of metal fell from in between the piston and cylinder, shown in Figure 5.4. It was determined that this was a piece of nickel leftover from the electroplating process. This small piece was initially attached to the underside of the piston, as shown in Figure 5.5. Before initially installing the piston in the engine, attempts were made to remove this piece of metal, but proved unsuccessful. It was decided at that time that the size and location of the small nickel piece were inconsequential and no further attempts were made to remove it.

Figure 5.4 and Figure 5.5. Leftover nickel piece causing engine damage, with penny shown for comparison and original location of nickel piece on piston skirt

5.2 Piston Embedded FBG Verification

The extent of the damage caused to the engine piston and cylinder caused concern about the durability of the embedded FBG. Before any further design changes or experiments were conducted, measurements were taken to verify that the FBG was still operational.

The piston and engine optics were assembled on the optical bench and were properly aligned. Figure 5.6 below shows the Bragg dips in the photodetector power trace. It was observed that the overall power transmission through the FBG was decreased by $\sim 10^3$. It was unsure what part of the observed decrease in transmission was due to misalignment and what was due to shock or strain effects caused by the loose nickel piece.

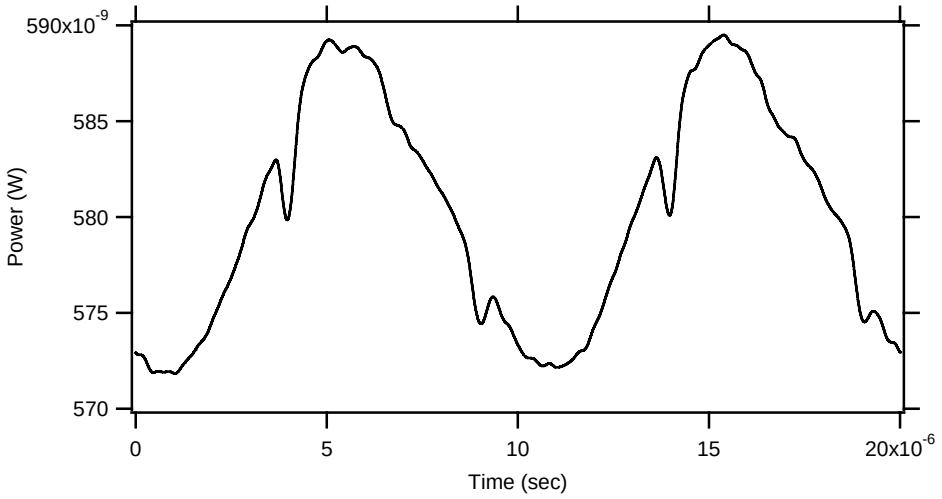

Figure 5.6. Transmitted VCSEL power through piston verifying Bragg dip

5.3 Modified Engine Setup

The damage caused by the loose piece of nickel eliminated the possibility of using the current engine to take piston temperature data for firing conditions. However, as the aim of this research was to prove the feasibility of the FBG measurement technique, modifications were made to the damaged engine and piston to make operation of the engine possible for a modified motoring condition.

The amount of metal buildup inside the engine cylinder required it to be rebored to a diameter of 68.50 mm. The reboring did not remove the deep gouge caused by the piston removal, but did remove much of the deposited aluminum piston material. The piston grooves were smoothed with a high-speed dental drill to remove the old damaged rings and make it possible for new rings to be installed. In addition, the outside surface of the piston was sanded and polished to remove any excess metal protrusions.

New rings were installed with notches to sit on the ring groove pins to keep the ring gaps clear of the optical windows. Thin metal shims made of 0.178 mm shim stock (see Figure 5.7) were installed in the piston ring grooves between the rings and piston. These shims were used to force the piston away from the cylinder walls to minimize piston slap and to keep the piston centered in the cylinder bore. The end gaps of the shims were located at the ring pin locations and the rings were installed over them.

Figure 5.7. Piston shims for centering piston in cylinder bore

The engine head was not reinstalled on the engine, since firing conditions were no longer being investigated. Leaving the head off of the engine also minimized the pressure forces acting on the piston. A piece of tape was used to cover the pushrod cavity to prevent any oil escape. After installing the engine on the laboratory dynamometer, only the crankcase vacuum and the shaft encoder were reconnected to the engine.

The engine was turned by hand to locate the position of maximum light transmission and the pitching optics were aligned also. The optical shaft encoder was installed on the engine such that the Z pulse signifying TDC occurred at the location of maximum light transmission, which was actually near BDC, providing a 5 V TTL trigger pulse for the oscilloscope. This installation made it possible to omit installing and aligning the 60 minus 6 timing wheel for the MotoTron engine control program.

5.4 Motoring Engine Investigation

Using the laboratory dynamometer, the Briggs engine was motored to 700 RPM and examined for possible mechanical problems and abnormal sounds indicating improper reassembly. While none were noticed, engine operation was monitored closely. As the piston and engine assembly warmed up, the pitching optics had to be continually adjusted to maintain light transmission through the piston. It was noticed that successful light coupling occurred on every rotation observed, indicating that the piston ring shims were forcing the piston to travel more consistently in the cylinder bore. From this observation, the oscilloscope was set to average 100 cycles of transmission data to minimize the large amplitude noise associated with the engine optical measurements.

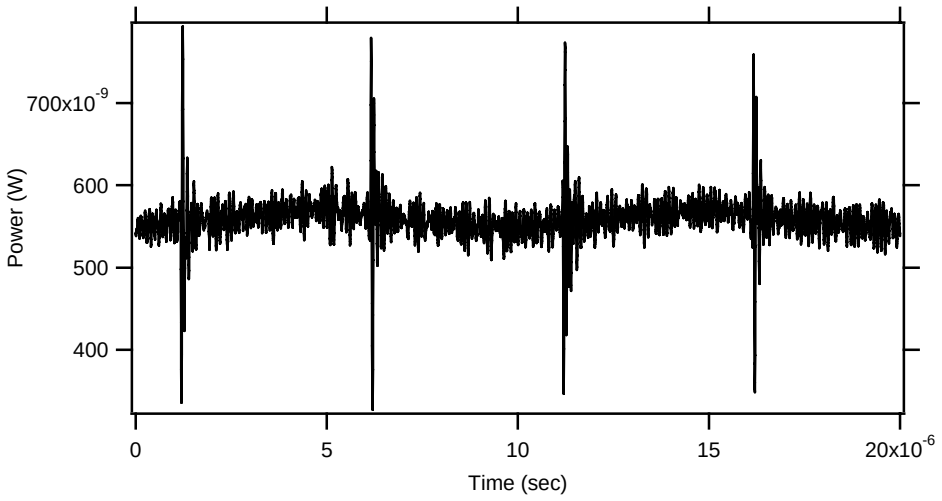

Figure 5.8. 100-times averaged light transmission through piston at 1000 RPM

Data were collected at speeds of 700 and 1000 RPM, chosen as slower speeds due to the condition of the experimental engine. The pitching optics could only be adjusted to maintain constant light transmission and not to maximize the Bragg dip since the levels of

power transmission were very low. Only after conducting a series of data manipulation procedures was the Bragg dip identified.

Figure 5.8 above shows a measured power profile averaged 100 times at an engine speed of 1000 RPM. The four sharp peaks are from the Sync output of the function generator providing the external modulation of the VCSEL diode. There is a significant amount of noise in this signal and the Bragg dip is not immediately noticeable. The data manipulation procedure explained in Chapter 4 was used to properly identify the Bragg wavelength location. Using these procedures, a plot of light transmission versus wavelength was generated and appears below in Figure 5.9.

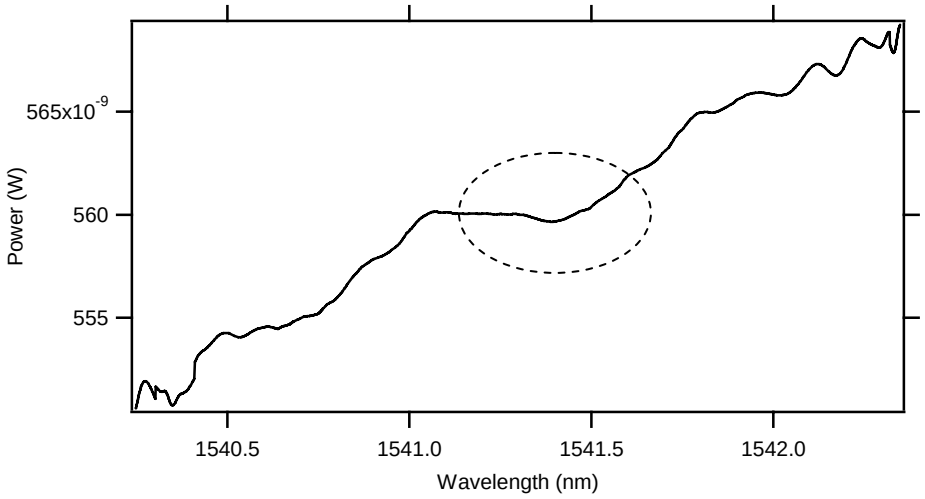

Figure 5.9. Measured transmitted optical power through piston FBG calibrated to VCSEL wavelength at 1000 RPM

Without knowing which region to look for the Bragg dip in, it is difficult to identify any one dip as the Bragg dip for this particular measurement. However, from the FBG temperature calibration a Bragg wavelength is expected in a domain from 1541 to 1542 nm.

Using this knowledge, the dip in this domain was identified at 1541.39 nm, corresponding to a piston temperature of 56.0 °C.

All other measurements taken during the motoring cases at 700 and 1000 RPM were extremely noisy and the analysis for determining Bragg wavelength and piston temperature was inconclusive. While the general VCSEL power profile was noticeable during engine operation, the level of noise caused by connecting the Sync signal for the triggering circuit masked the underlying light transmission signal.

6 Conclusions and Recommendations

The analyses conducted on each aspect of the non-intrusive piston temperature measurement project provided insight into ways of improving optical transmission efficiency through optical design, embedding technique and measurement procedure.

6.1 Optical Design

Coupling light efficiently into a 9 μm fiber was an inherently difficult process. From experiments conducted with air gaps comparable to those found in the engine, it was determined that a collimating lens would improve coupling efficiency and provide a more flexible means of locating the pitched light. This modification had the negative impact of decreasing the spot size of the incoming light as compared to the spot created without the lens. However, by specifying the required pitched spot size, a system of equations was solved to determine the required locations of the collimating lens and pitching fiber. Using a collimating lens decreased the divergence angle of the incoming light, which decreased the variance of the measured Bragg wavelength and increased the amount of light transmitted.

On the collection side, a possible improvement would be to incorporate an X-Y or X-Y-Z translation assembly to provide additional means of maximizing overall coupling efficiency. Such an apparatus could also be fabricated from standard optical parts and designed to coincide with the existing collection window fixture attached to the engine.

6.2 Fiber Bragg Grating Embedding Technique

Measurements made on bare and buffered fibers indicated that maintaining a buffer on the embedded FBG greatly improved the depth of the Bragg dip and eliminated the hindrance caused by cladding modes. Bare fibers were originally used due to the low temperature tolerance of the standard acrylate buffer. Fibers buffered with polyimide, which was rated for operating temperatures up to 200 °C, were installed in the piston without having to mechanically remove the buffer and possibly damage the FBG fiber. The engine damage incurred made it impossible to conduct firing engine tests, and made examining the survivability of the polyimide buffer impossible as well. Future experiments should be conducted to examine the effects of high temperatures on the polyimide buffered FBG embedded in the piston.

In addition to buffer materials, different methods of attaching the FBG to the piston were examined. The procedure conducted by D. Ward to attach the FBG fiber to the piston relied on coating the FBG with thin layers of titanium and nickel to allow bonding with the electroplated metal. Since the metal sputtering technique was not utilized in this research, an alternative study of fiber embedding involving epoxies was conducted. By using a small amount of optically absorptive epoxy on the pitching side of the piston, the FBG was securely fastened while also providing a means to attenuate stray light not traveling through the FBG fiber.

The optically absorptive epoxy was rated at a continuous operating temperature of 225 °C and an intermittent temperature of 325 °C. As was the case with the polyimide buffer, the temperature limits were not able to be investigated due to the damage sustained by the

engine. A recommended experiment would use the piston with an epoxy-embedded fiber at firing engine conditions. Measurements of the optical transmission efficiency over time as well as a final wear test would prove beneficial in determining the robustness of the embedding technique.

6.3 Measurement Procedure

During the engine motoring experiments, it was noticed that light transmission was occurring during each engine revolution. Considering the extent of damage to the engine, the observed repeatability of the measurements partially validated both the redesigned pitching optics and the modified fiber embedding process. However, the measured power profile was obscured by four sharp spikes, as previously shown in Figure 5.8. The photodetector power trace on the oscilloscope showed the spikes when the Sync output from the function generator was connected to the oscilloscope triggering circuit. As a result, analyzing the measured data was difficult and in the end was inconclusive. Isolating the spikes from the measured transmitted power would allow more bits for quantization while also providing for increased signal averaging.

References

[1] Sitkei, György, 1974, *Heat Transfer and Thermal Loading in Internal Combustion Engines*, Akadémiai Kiadó, Budapest.

[2] Heywood, John B., 1988, *Internal Combustion Engine Fundamentals*, McGraw-Hill, New York.

[3] Burrahm, R.W., Davis, J. K., Perry, W. D., De Los Santos, A., 1992, "Development of a Piston Temperature Telemetry System," SAE 920232

[4] Barna, G.L., Brumm, D.B., Anderson, C.L., 1991, "Infrared Telemetry Technique for Making Piston Temperature Measurements," SAE 910051

[5] Rollwitz, W.L. and Lawrason, G.C., 1967, "A Temperature Telemetry Technique for Reciprocating Engines," SAE 670026

[6] Furuhama, S., Tada, T., Nakamura, T., 1964, "Some Measurements of the Piston Temperatures in a Small Type Gasoline Engine," *Bulletin of the JSME*, v. 7 no. 26 pp. 422-429

[7] Baker, H.W., 1934, "Operating Temperatures of Cast Iron and Aluminum Pistons in 12-Inch Bore Oil Engine," *Proceedings of the Inst. of Mechanical Engineers*, v. 127 pp. 217-243

[8] Pinski, F.I., 1964, "Temperature Measurement of Internal-Combustion Engine Pistons," *Measurement Techniques*, no. 7

[9] Takamatsu, H., Kanazawa, T., 1999, "Piston Temperature Measurement Method for High-Speed Gasoline Engines," *JSAE Review*, v. 20 is. 2 pp. 259-261

[10] Underwood, A.F. and Catlin, A.A., 1941, "Instrument for Continuous Measurement of Piston Temperatures," *SAE Journal*, v. 48 is.1 pp. 20-27

[11] Yoshihiko, I., Tanaka, K, Fuse, S., 1983, "Contact-point Method for Measuring Sliding Face Temperature and Its Applications," SAE 830311

[12] Opris, M.C., Jason, R.R., Anderson, C.L., 1998, "Comparison of Time-Averaged Piston Temperatures and Surface Heat Flux Between a Direct-Fuel Injected and Carbureted Two-Stroke Engine," SAE 980763

[13] Kato, N., Moritsugu, M., Shimura, T., Matsui, J., 2001, "Piston Temperature Measuring Technology Using Electromagnetic Induction," SAE 2001-01-2027

[14] TEMPLUG User Information Guide, April 2004, Revision 3.0

[15] Hill, K.O., Fujii, Y., Johnson, D.C., Kawasaki, B.S., 1978, "Photosensitivity in Optical Fiber Waveguides: Application to Reflection Filter Fabrication," *Applied Physics Letters*, v. 32 is. 10 pp. 647-649

[16] Othonos, A. and Kalli, K., 1999, *Fiber Bragg Gratings: Fundamentals and Applications in Telecommunications and Sensing*, Artech House, Boston

[17] Maaskant, R., et.al., 1997, "Fiber-Optic Bragg Grating Sensors for Bridge Monitoring," *Cement & Concrete Composites*, v. 19 is. 1 pp. 21-33, Toronto

[18] Li, X. and Prinz, F., 2004, "Analytical and Experimental Study on Non-Contact Sensing with Embedded Fiber Optic Sensors in Rotating Metal Parts," *Journal of Lightwave Technology*, v. 22 is. 7 pp. 1720-1727, Piscataway

[19] Frazão, O., Ferreira, L.A., Araújo, F.M., Santos, J.L., 2005, "Simultaneous Measurement of Strain and Temperature Using Fiber Bragg Gratings in a Twisted Configuration," *Journal of Optics A: Pure and Applied Optics*, v. 7 is. 8 pp. 427-430, Bristol, UK

[20] Yu, F. and Yin, S., 2002, *Fiber Optic Sensors*, Marcel Dekker, New York

[21] Zhang, W., *et. al.*, 2005, "Novel Temperature-Independent FBG-Type Force Sensor," *Measurement Science and Technology*, v. 16 is. 8 pp. 1600-1604, Bristol, UK

[22] Hill, K.O. *et. al.*, 1993, "Bragg Gratings Fabricated in Monomode Photosensitive Optical Fiber by UV Exposure through a Phase Mask," *Applied Physics Letters*, v. 62 is. 10 pp. 1035-1037, Melville, New York

[23] Yunming, W. *et. al.*, 2005, "Theoretical and Experimental Study on Multimode Optical Fiber Grating," *Optics Communications*, v. 250 is. 1-3 pp. 54-62, Amsterdam

[24] Ward, D., 2004, "Engine Piston Temperature Measurements for Thermal Loading using a Fiber Bragg Grating (FBG) Embedded Into the Piston Surface," M.S. Thesis, Mechanical Engineering Department, University of Wisconsin – Madison

[25] Degamber, B., Tetlow, J, Fernando, G.F., 2004, "Design and Development of Low-Cost Optical-Fiber Sensors for Temperature Metrology: Process Monitoring of an Epoxy Resin System," *Journal of Applied Polymer Science*, v. 94 is. 1 pp. 83-95

[26] Perez, M.A. *et. al.*, 2001, "A New Monitorization System to Measure Metals Dissolved in Water by Means of Room-Temperature Phosphorescence Optical Fiber Sensors," *IEEE Inst. and Meas. Tech. Conf.*, Budapest, Hungary

[27] Omrane, A., Ossler, F., Aldén, M., 2004, "Temperature Measurements of Combustible and Non-Combustible Surfaces Using Laser Induced Phosphorescence," *Experimental Thermal and Fluid Science*, v. 28 pp. 669-676

[28] Aizawa, H. *et. al.*, 2002, "Fiber-optic Thermometer Using Afterglow Phosphorescence from Long Duration Phosphor," *Electrochemical and Solid-State Letters*, v. 5 is. 9 pp. H17-H19

[29] Feist, J.P. *et. al.*, 1999, "Phosphor Thermometry for High Temperature Gas Turbine Applications," ICIASF '99: 18th International Conference on Instrumentation in Aerospace Simulation Facilities, Toulouse Cedex, France, June 14-17 1999, pp. 6-7, Piscataway, NJ, IEEE

[30] Husberg, T. *et. al.*, 2005, "Piston Temperature Measurement by Use of Thermographic Phosphors and Thermocouples in a Heavy-Duty Diesel Engine Run under Partly Premixed Conditions," SAE 2005-01-1646

[31] Särner, G. *et. al.*, 2005, "Cycle Resolved Wall Temperature Measurements using Laser-Induced Phosphorescence in an HCCI Engine," SAE 2005-01-3870

[32] Morse, K., 1996, "Piston Temperature Measurements for a Two-Stroke Spark Ignition Engine Using an Infrared Telemetry Technique," M.S. Thesis, Michigan Technological University

[33] Dembroski, T., 2002, "Piston Heat Transfer in an Air-Cooled Engine," M.S. Thesis, Mechanical Engineering Department, University of Wisconsin – Madison

[34] Albert, B., 2004, "Residual Gas Effects on Combustion in an Air-Cooled Utility Engine," M.S. Thesis, Mechanical Engineering Department, University of Wisconsin – Madison

Appendix A – Computer Codes

A.1 IGOR procedure file for transverse analysis

```
Function Attenuation(sig0,ref0)
	wave sig0;		// Signal wave
	wave ref0;		// Reference wave
	Variable x1;
	Variable x2;
	Variable avg0, diff1;
	Variable band1, band2, bandwidth;
	Variable n_pts;

	// smooth 15,sig0;
	WaveStats /Q sig0;
	n_pts = V_npnts + V_numNans + V_numINFs;

	Make/O/N=(n_pts) att0;
	att0 = 10 * log(sig0/ref0)
	CopyScales ref0 att0;
	x1 = leftx(att0);
	x2 = rightx(att0);
	avg0 = mean(att0,x1,x2);
	Print "Average loss: ",avg0, " dB";

	Make/O/N=(n_pts) avg_wave;
	avg_wave = avg0;
	CopyScales ref0 avg_wave;

	Display att0 as "Signal Loss Versus Reference";
	Label left "Attenuation (dB)\\Z16";
	Label bottom "Wavelength (nm)\\Z16";
	SetAxis/A;

End
```

A.2 IGOR procedure file for etalon correlation

```
#pragma rtGlobals=1             // Use modern global access method.

Function peakcount(etalon,osa)
        wave    etalon,osa;
        variable freq,temp;     // freq in kHz, temp in C
        variable i,dx,num;
        string  waven_actual;
        string  waven_osa;
        string  tuningn;
        variable low_nu,high_nu;
        variable low_lambda,high_lambda;
        variable num_peaks,ctr,approx_loc;
        variable start,stop;
        string  fsr;

        freq = 100;
        temp = 20;
        duplicate /O etalon,ave_etalon,ref_etalon;
        smooth /E=1/B=30 10,ave_etalon;
        ref_etalon = etalon/ave_etalon;
        //smooth /e=1/b=10 5,ref_etalon;

        differentiate ref_etalon /D=diff_etalon2;

        smooth /e=1/b=2 5,diff_etalon2;
        findlevels diff_etalon2,0;
        duplicate /O W_findlevels,wfindlevels,testfindlevels;

        duplicate /O etalon,wavenmap2;
        dx = deltax(wavenmap2);
        num = numpnts(wavenmap2);
        for(i=0;i<num;i+=1)
                findlevel /Q W_findlevels, (i*dx);
                wavenmap2[i] = V_levelx;
        endfor

        differentiate W_findlevels /d=diff_findlevels;
        smooth 20,diff_findlevels;
        killwindow DiffGraph1;
        display /N=DiffGraph1 /W=(5.25,42.5,909,251) diff_findlevels;
        ModifyGraph nticks(bottom)=8;
        ModifyGraph minor(bottom)=1;
        ModifyGraph sep(bottom)=10;
        doupdate;

        wavestats /q diff_findlevels;
        findlevels /q diff_findlevels,(0.65*V_max);
        num_peaks = (V_levelsfound / 2);
        prompt  num_peaks, "num_peaks:";
        doprompt "Enter number of peaks (reversals) in trace", num_peaks;
```

```
	make /o/n=30 reversal;
	deletepoints num_peaks,30,reversal;

	wavestats /q/r=(0,(rightx(diff_findlevels)/num_peaks)) diff_findlevels;
	approx_loc = V_maxloc;
	for (ctr=1;ctr<=num_peaks;ctr+=1)
		prompt  approx_loc, "Location:";
		doprompt ("Approximate location of peak number " + num2str(ctr)), approx_loc;
		wavestats /Q/R=(approx_loc-20,approx_loc+20) diff_findlevels;
		reversal[ctr-1] = wfindlevels(V_maxloc);
		approx_loc += (rightx(diff_findlevels)/(num_peaks));

	endfor

	duplicate /O wavenmap2,wavereversal;
	for (ctr=1;ctr<=num_peaks;ctr+=2)
		start = x2pnt(wavereversal,reversal[ctr-1]);
		stop = x2pnt(wavereversal,reversal[ctr]);
		wavereversal[start,stop] = 2*wavereversal[start]-wavereversal[p];
		wavereversal[stop, ] = wavereversal[p] - 2*(wavereversal[stop] - wavereversal[start]);
		//return 0;
	endfor

	//  This block is for pegging the wavlength to the osa trace

		wavestats /q osa
		findlevels /q osa,(0.5*V_avg);
		duplicate /O W_findlevels,wfindlevels;
		start = wfindlevels[0] - 0.5;
		stop = wfindlevels[1] + 0.5;
		wavestats /q/r=(start,(stop-start)/3+start) osa;

		low_lambda = V_maxloc;
		low_nu = 10^7/low_lambda;
		wavestats /q/r=((2/3)*(stop-start),stop) osa;
		high_lambda = V_maxloc;
		high_nu = 10^7/high_lambda;

	print "Low wavelength is",low_lambda,"nm\tLow wavenumber is",low_nu,"cm-1";
	print "High wavelength is",high_lambda,"nm\tHigh wavenumber is",high_nu,"cm-1";

	fsr = "fsr" + num2str(freq) + "kHz";
	duplicate /O wavereversal,$fsr;

	killwaves test_w,ave_etalon,ref_etalon;
End
```

```
Function avetest(num_cycles,w_name,fsr)
	variable num_cycles;
	wave     w_name,fsr;
	variable total,start_p,num_p;
	variable ctr,ctr2;

	duplicate /o w_name,avephotod,fsr_ave;
	avephotod = 0;
	fsr_ave = 0;
	total = numpnts(w_name);
	wavestats /q /r=[0,(total*2)/num_cycles] fsr;
	start_p = x2pnt(fsr,min(V_minloc,V_maxloc));
	num_p = abs(x2pnt(fsr,V_maxloc)-x2pnt(fsr,V_minloc));
	deletepoints num_p,total,avephotod,fsr_ave;
	fsr_ave = fsr[p+start_p];
	for (ctr=0;ctr<=num_p;ctr+=1)
		findlevels/p/q fsr,fsr_ave[ctr];
		duplicate/o W_FindLevels,wlevels;
		for (ctr2=0;ctr2<V_LevelsFound;ctr2+=1)
			avephotod[ctr] +=(1/V_LevelsFound)*w_name[wlevels[ctr2]];
		endfor
	endfor


End

Function fsrscale(fsr)
	wave     fsr;
	variable low_nu,high_nu;

	prompt low_nu, "Low nu:";
	prompt high_nu, "High nu:";
	doprompt "Enter wavenumbers for start and end of VCSEL trace",low_nu,high_nu;
	wavestats /q fsr;
	fsr -= V_min;
	wavestats /q fsr;
	fsr /= V_max;
	fsr*=(low_nu-high_nu);
	fsr+=high_nu;
	fsr = 10^7/(fsr);

End
```

A.3 MATALB code for Gaussian optics calculations

```
% gauss2.m
% Timothy Pfeifer
% Created:  November 28, 2005
% Modified: May 15, 2006
%
% Gaussian optics calculations for determining:
% 1)  Lens focal length
% 2)  Distances between optics
% For use in FBG optical piston experiment

hold off;

x2 = 700:10:110000; % micron

omega_0_2 = 300;    % micron, desired spot size on piston
wavelength = 1550;  % nm, operating wavelength
lambda = wavelength/1000;   % micron
x_R_2 = (pi*omega_0_2^2)/lambda;    % micron,
q_bar_0_2 = x_R_2*i;    % micron * i
omega_2 = omega_0_2*sqrt(1+(x2/x_R_2).^2);  % micron
R_2 = x2 + (x_R_2^2)./x2;   % micron;
q_bar_2 = 1./((1./R_2) - i*(lambda./(pi*omega_2.^2)));  % micron * i

f1 = 6.16*1000; % micron, lens focal length

q_bar_f1 = 1./((1./q_bar_2) + 1/f1);    % micron * i, lens transformation

x_lens_f1 = real(q_bar_f1)./1000;   % mm, waist location determined by
lens

% Single mode pitching
omega_0_1 = 9;  % micron
x_R_1 = (pi*omega_0_1^2)/lambda;    % micron
x_lens = x_R_1*sqrt((omega_2./omega_0_1).^2-1); % micron
x_lens_plot = x_lens ./1000;    % mm

x_plot = x2./1000;  % mm
plot(x_plot,x_lens_plot,'k',x_plot,x_lens_f1,'b');
legend('Waist matching at lens','Complex radius matching at
lens','location','West');
title(['Spot size: ' num2str(omega_0_2) ' micron , f1 = ' num2str(f1/1000)
' mm, Wavelength: ' num2str(wavelength) ' nm']);
xlabel('x2 [mm]');
ylabel('x1 [mm]');

% Solve for intersection
x2_sol_index = min(find(x_lens_f1<=x_lens_plot));
x2_sol = x_plot(x2_sol_index);
x1_sol = x_lens_f1(x2_sol_index);
```

```
x1_sol_2 = x_lens_plot(x2_sol_index);
hold on;
plot(x2_sol,x1_sol,'ro');

disp(['Solution for wavelength of ' num2str(wavelength) ' nm']);
disp(['Spot size: ' num2str(omega_0_2) ' micron']);
disp(['Lens focal length (f): ' num2str(f1/1000) ' mm']);
disp('Solution:');
disp(['x1 = ' num2str(x1_sol,'%0.7g') ' mm (' num2str(x1_sol_2,'%0.7g') '
mm)']);
disp(['x2 = ' num2str(x2_sol,'%0.7g') ' mm']);

hold off;
```

Appendix B – Additional Figures

B.1 Modulated current VCSEL operation

B.1.1 Actual VCSEL Current Measured from VCSEL Control Board

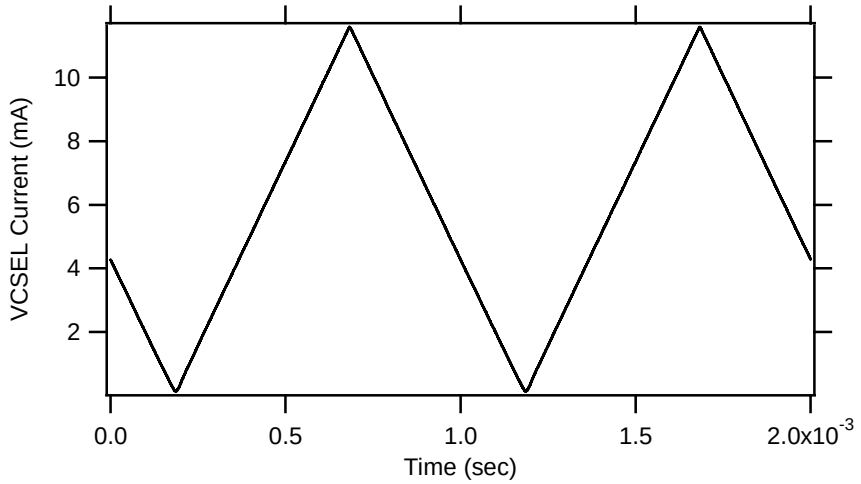

Figure B.1 Actual VCSEL current at modulation frequency of 1 kHz

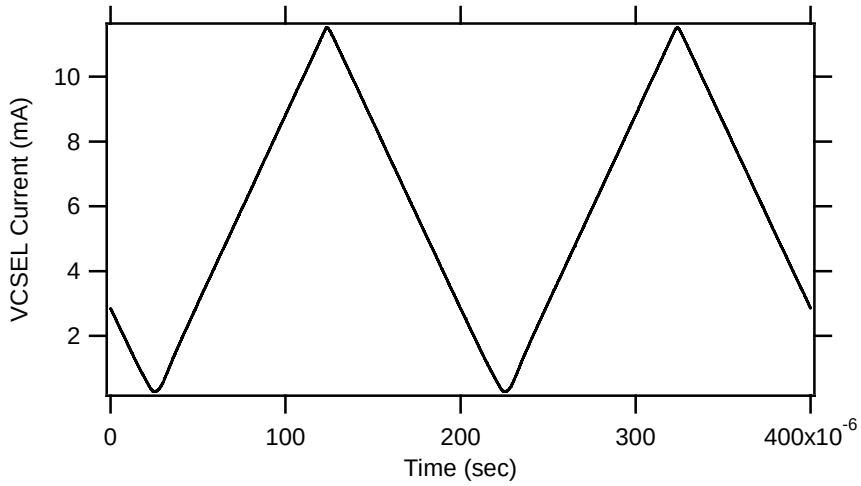

Figure B.2. Actual VCSEL current at modulation frequency of 5 kHz

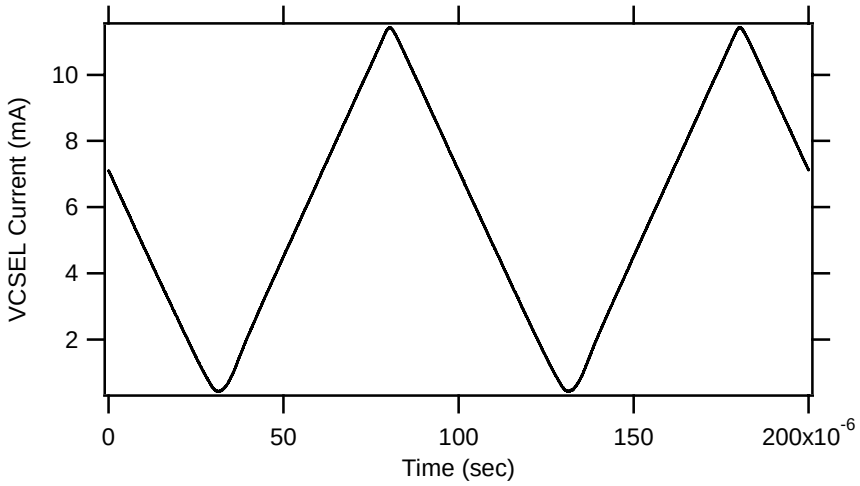

Figure B.3. Actual VCSEL current at modulation frequency of 10 kHz

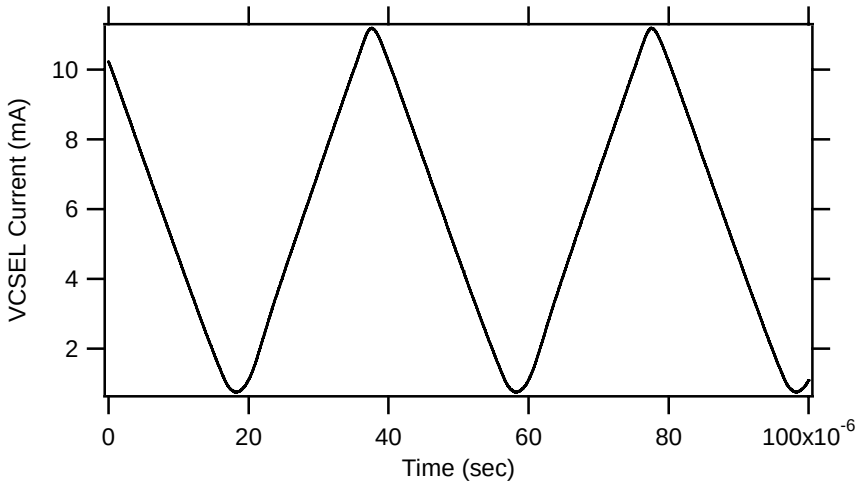

Figure B.4. Actual VCSEL current at modulation frequency of 25 kHz

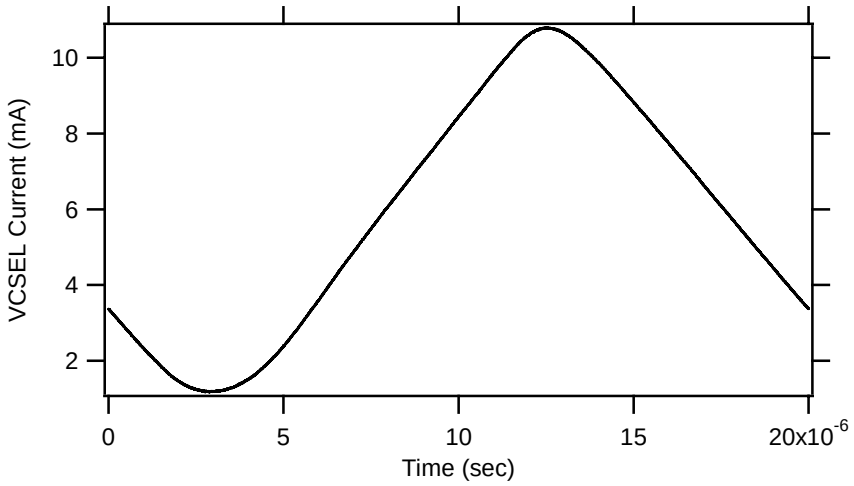

Figure B.5. Actual VCSEL current at modulation frequency of 50 kHz

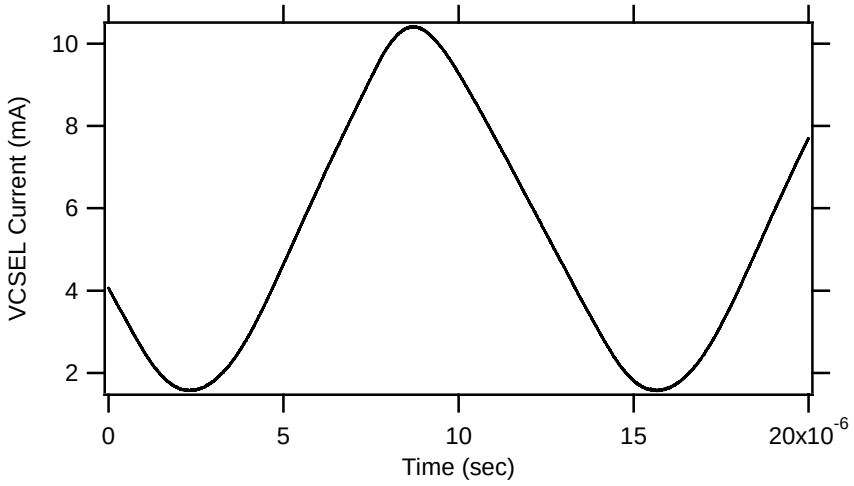

Figure B.6. Actual VCSEL current at modulation frequency of 75 kHz

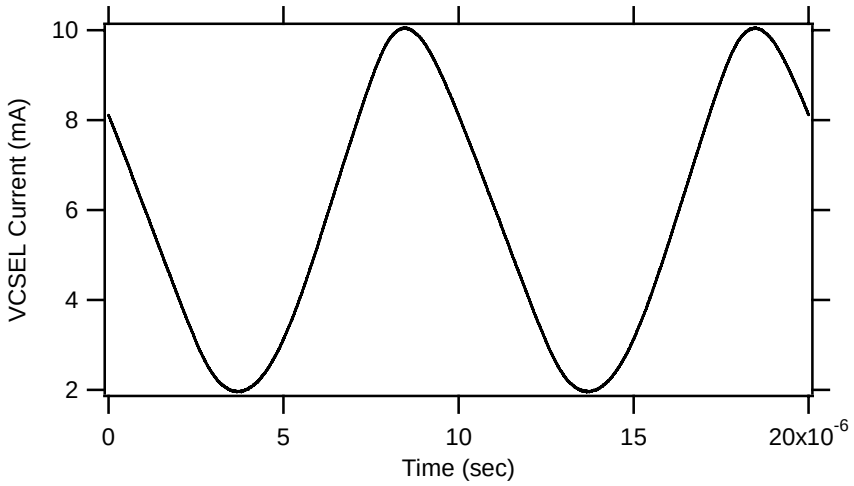

Figure B.7. Actual VCSEL current at modulation frequency of 100 kHz

B.1.2 Measured VCSEL Power through Polyimide Fiber Bragg Grating

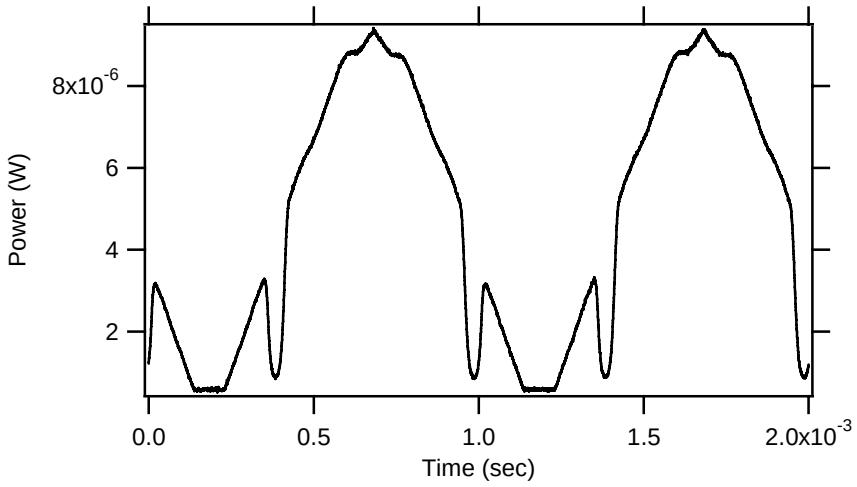

Figure B.8. Measured VCSEL power through FBG at modulation frequency of 1 kHz

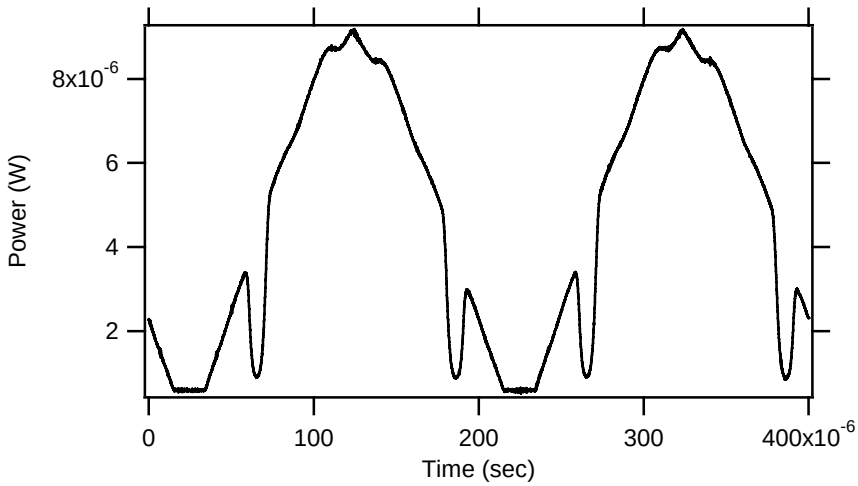

Figure B.9. Measured VCSEL power through FBG at modulation frequency of 5 kHz

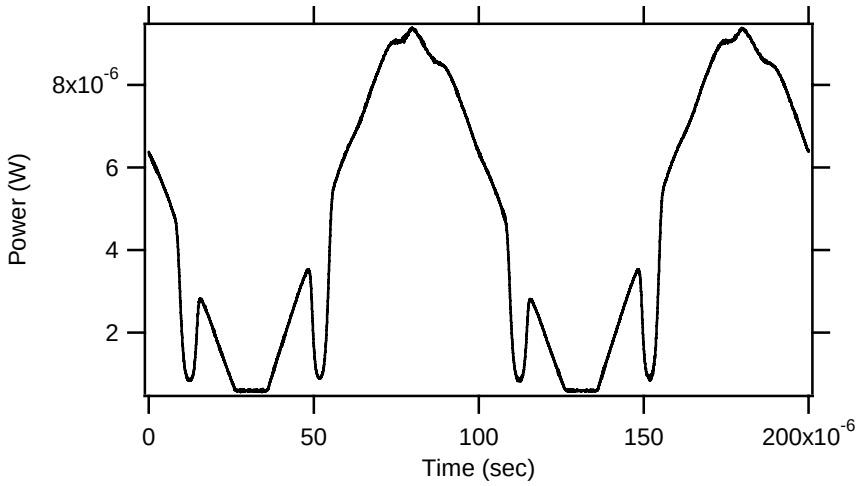

Figure B.10. Measured VCSEL power through FBG at modulation frequency of 10 kHz

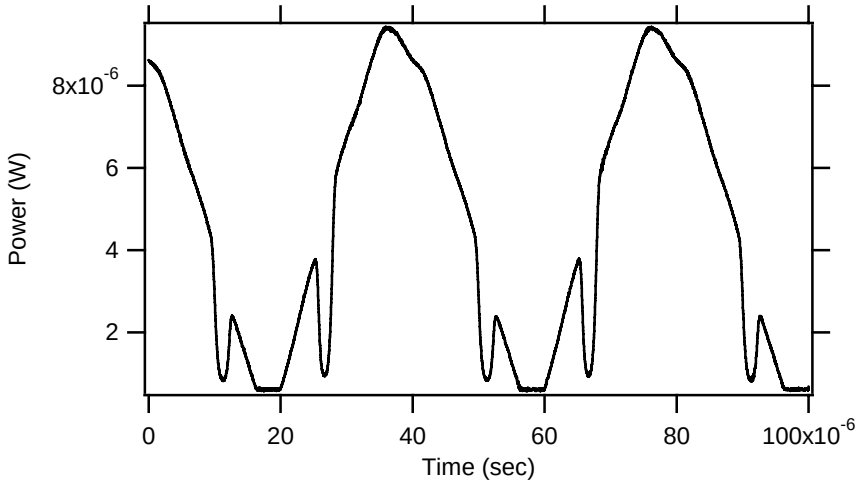

Figure B.11. Measured VCSEL power through FBG at modulation frequency of 25 kHz

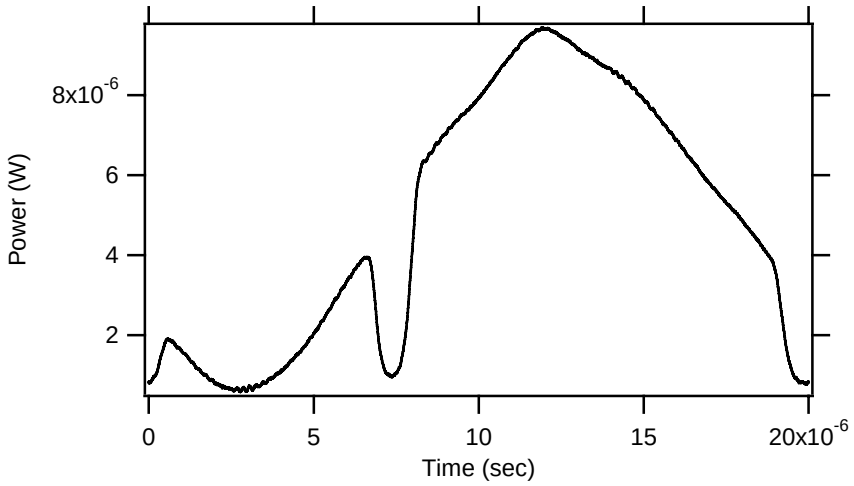

Figure B.12. Measured VCSEL power through FBG at modulation frequency of 50 kHz

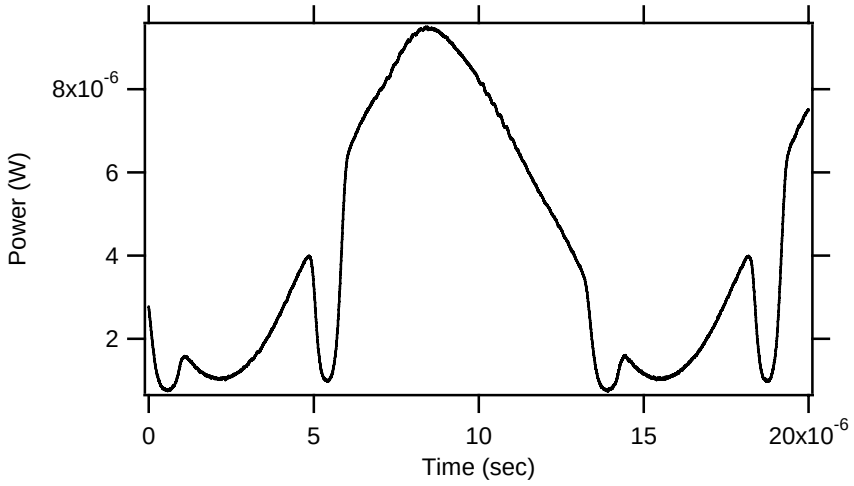

Figure B.13. Measured VCSEL power through FBG at modulation frequency of 75 kHz

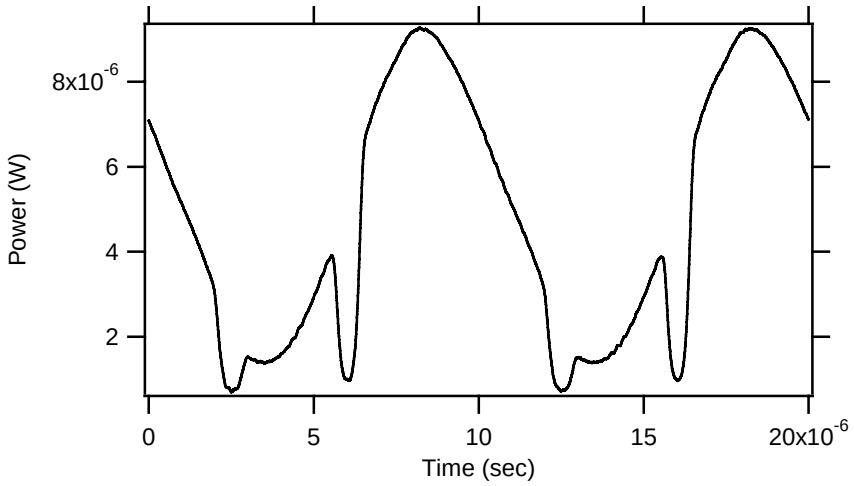

Figure B.14. Measured VCSEL current through FBG at modulation frequency of 100 kHz

B.2 Correlated Bragg wavelengths for temperature calibration

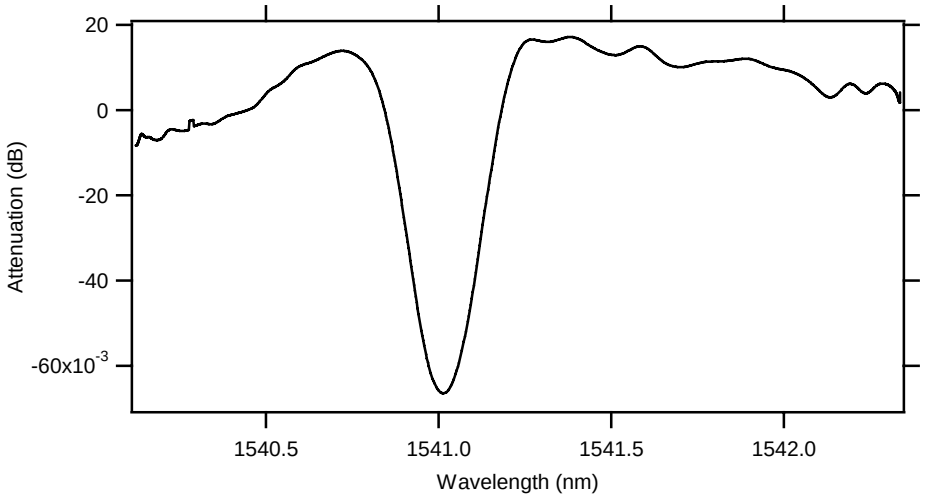

Figure B.15. Bragg dip for piston temperature of 24 °C

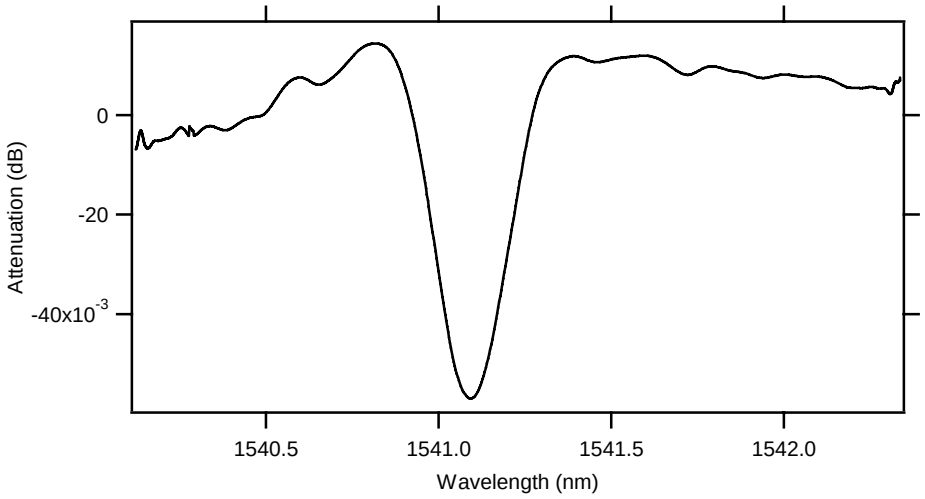

Figure B.16. Bragg dip for piston temperature of 30 °C

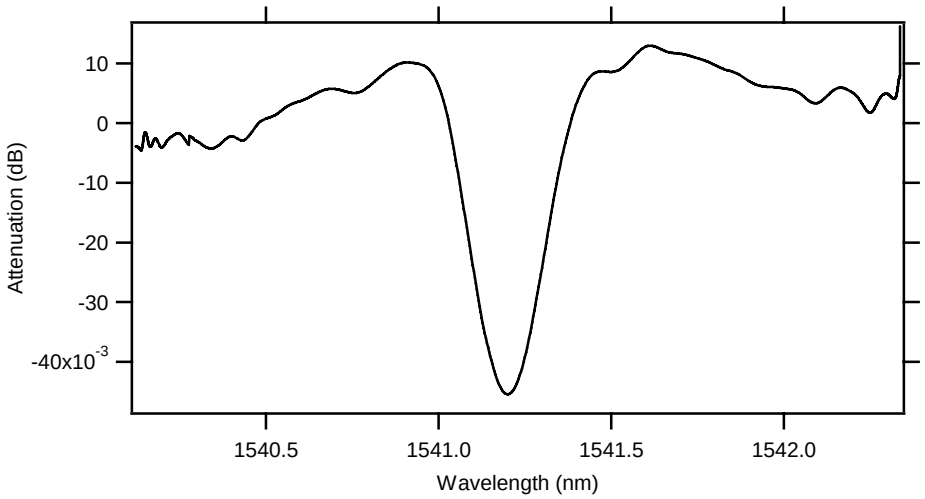

Figure B.17. Bragg dip for piston temperature of 40 °C, Scan 1

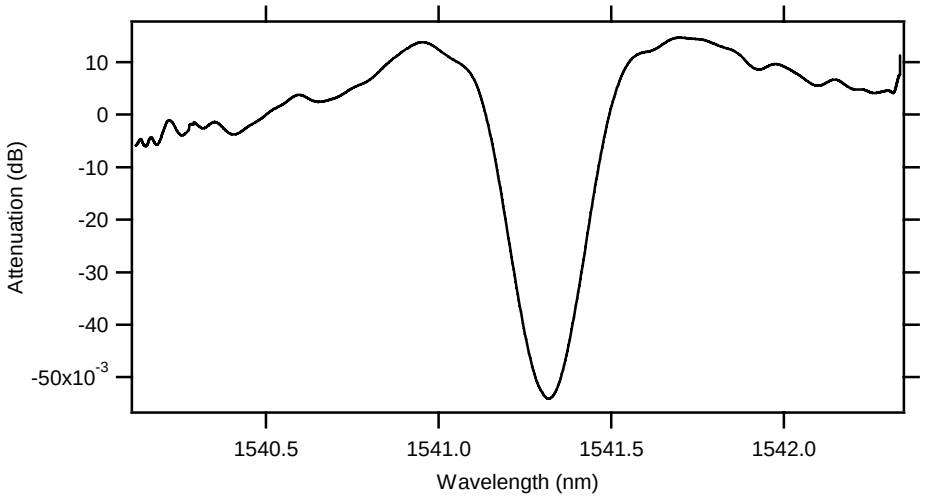

Figure B.18. Bragg dip for piston temperature of 50 °C, Scan 1

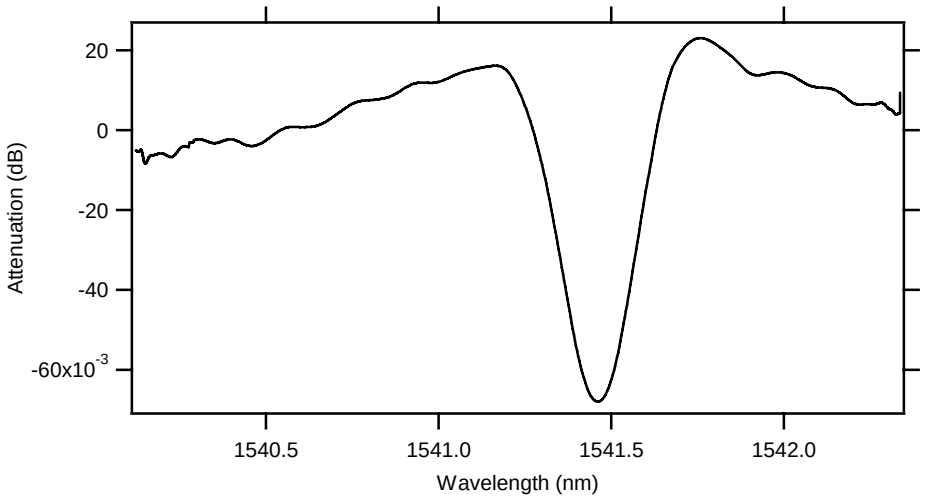

Figure B.19. Bragg dip for piston temperature of 60 °C, Scan 1

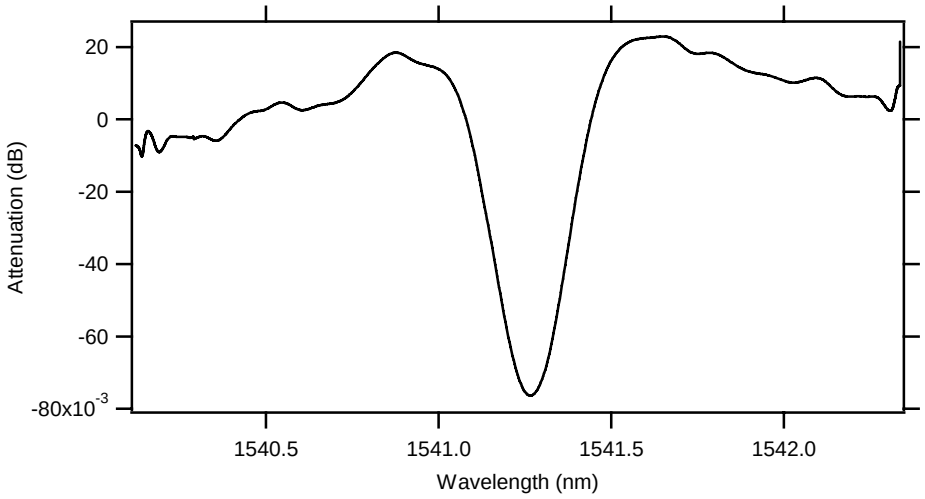

Figure B.20. Bragg dip for piston temperature of 50 °C, Scan 2

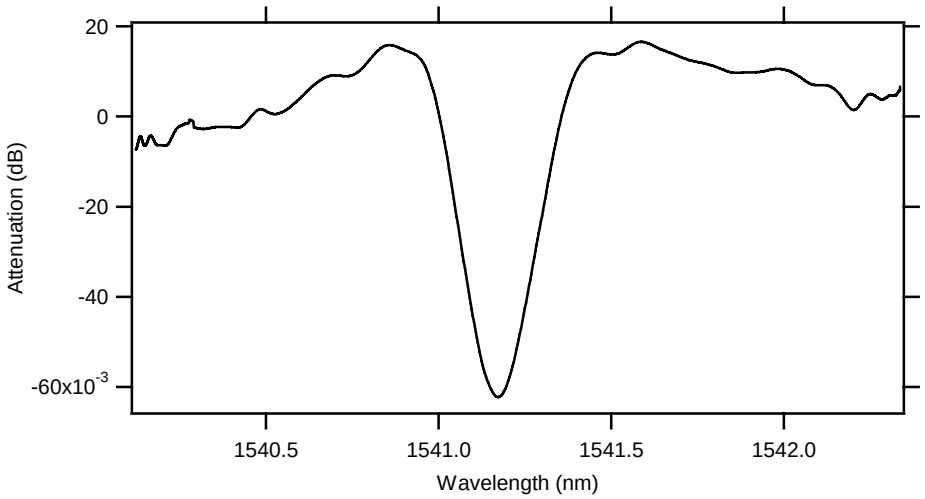

Figure B.21. Bragg dip for piston temperature of 40 °C, Scan 2